

Nucleosynthesis in magneto-rotational supernovae

M. Reichert,^{1,2} M. Obergaulinger,^{1,3} M. Eichler,¹ M. Á. Aloy,³ and A. Arcones^{1,2,4} 

¹*Institut für Kernphysik, Technische Universität Darmstadt, Schlossgartenstr. 2, Darmstadt 64289, Germany*

²*Helmholtz Forschungsakademie Hessen für FAIR, GSI Helmholtzzentrum für Schwerionenforschung, 64291 Darmstadt, Germany*

³*Departament d'Astronomia i Astrofísica, Universitat de València, Edifici d'Investigació Jeroni Munyoz, C/Dr. Moliner, 50, E-46100 Burjassot (València), Spain*

⁴*GSI Helmholtzzentrum für Schwerionenforschung GmbH, Planckstr. 1, Darmstadt 64291, Germany*

Accepted XXX. Received YYY; in original form ZZZ

ABSTRACT

We present the nucleosynthesis of magneto-rotational supernovae (MR-SNe) including neutrino-driven and magneto-rotational-driven ejecta based, for the first time, on 2D simulations with accurate neutrino transport. The models analysed here have different rotation and magnetic fields, allowing us to explore the impact of these two key ingredients. The accurate neutrino transport of the simulations is critical to analyse the slightly neutron-rich and proton-rich ejecta that are similar to the, also neutrino-driven, ejecta in standard supernovae. In the model with strong magnetic field, the r-process produces heavy elements up to the third r-process peak ($A \sim 195$), in agreement with previous works. This model presents a jet-like explosion with proton-rich jets surrounded by neutron-rich material where the r-process occurs. We have estimated a lower limit for ^{56}Ni of $2.5 \times 10^{-2} M_{\odot}$, which is still well below the expected hypernova value. Longer simulations including the accretion disc evolution are required to get a final prediction. In addition, we have found that the late evolution is critical in a model with weak magnetic field in which late-ejected neutron-rich matter produces elements up to the second r-process peak. Even if we cannot yet provide conclusions for hypernova nucleosynthesis, our results agree with observations of old stars and radioactive isotopes in supernova remnants. This makes MR-SNe a good additional scenario to neutron star mergers for the synthesis of heavy elements and brings us closer to understand their origin and the role of MR-SNe in the early Galaxy nucleosynthesis.

Key words: MHD - nuclear reactions, nucleosynthesis, abundances - supernovae: general - gamma rays: general

1 INTRODUCTION

Core-collapse supernovae are critical for the chemical history of the universe. These explosive events at the end of the life of massive stars enrich the interstellar medium with alpha elements, iron group elements, and probably heavier ones. What are the heaviest elements that can be produced in core-collapse supernovae? This depends on how the matter is ejected. Standard supernovae are driven by neutrinos (see e.g., Janka et al. 2016; Müller 2020; Kotake et al. 2012, for recent reviews) that determine the conditions of the ejecta, namely electron fraction (Y_e), entropy, and expansion time-scale. The ejecta can be slightly neutron-rich ($Y_e < 0.5$) and/or proton rich ($Y_e > 0.5$). In both cases, elements up to Sr, Y, Zr may be produced (Arcones & Thielemann 2013; Arcones & Bliss 2014; Wanajo et al. 2018). Alternatives to this standard mechanism have been suggested to explain very energetic supernovae, some of which are associated with long gamma-ray bursts (GRBs) producing relativistic outflows (Nomoto et al. 2006; Woosley & Bloom 2006; Cano et al. 2017; Moriya et al. 2018). Since by themselves, neutrino heating and hydrodynamic instabilities have difficulties powering these extreme events, rapid rotation and strong magnetic fields have been invoked to ex-

plain these events (Wheeler et al. 2002; Maeda & Nomoto 2003; Dessart et al. 2008; Tominaga 2009; Metzger et al. 2011; Dessart et al. 2012; Mazzali et al. 2014; Metzger et al. 2015, 2018; Aloy & Obergaulinger 2020). Further indications for the importance of magnetic fields in a subset of all supernovae come from the observation of very strongly magnetized, young neutron stars, so-called magnetars (Duncan & Thompson 1992; Kaspi & Beloborodov 2017). If combined with high rotational energies, newly born magnetars (also known as *protomagnetars*) could inject energy at high rates into the ejecta and power very violent explosions, thereby spinning down to their observed, rather long rotation periods (Metzger et al. 2011). This explosion mechanism has not attracted the same attention as standard explosions (but see Aloy & Obergaulinger 2020, who show evidences of protomagnetar formation more than 5 s after the core bounce of low-metallicity, massive, stellar progenitors endowed with sufficiently strong poloidal magnetic fields). Partly, this is due to numerical difficulties such as the necessity to resolve small-scale structures of the flow and the field generated by, e.g., the magnetorotational instability (Obergaulinger et al. 2009; Rembiasz et al. 2016a,b). Additionally, the required rotation rates and magnetic energies restrict this mechanism to a minority of progenitor stars and, thus, observed explosions.

Despite their relatively small numbers, magneto-rotational supernovae (MR-SNe) may nevertheless be important contributors to the enrichment of galaxies with heavy elements in the early universe (Côté et al. 2019). In addition to neutrino-driven ejecta, these ex-

* E-mails:

mreichert@theorie.ikp.physik.tu-darmstadt.de

miguel.a.aloy@uv.es

almudena.arcones@physik.tu-darmstadt.de

plosions have an early and fast ejection of matter where the rapid neutron capture process (r-process) can efficiently produce heavy elements (Nishimura et al. 2006; Winteler et al. 2012; Saruwatari et al. 2013; Nishimura et al. 2015, 2017; Mösta et al. 2018), similarly to the prompt explosions found in the 70s (Hillebrandt et al. 1976). Here we present the first nucleosynthesis study based on 2D supernova simulations with accurate neutrino transport (Obergaullinger & Aloy 2017, 2020b; Aloy & Obergaullinger 2020). Therefore, we can uniquely and consistently study the nucleosynthesis of both neutrino-driven and magnetic-driven ejecta within the same supernova model.

The nucleosynthesis in core-collapse supernovae have been extensively studied for alpha and iron group elements based on simple models (see e.g., Woosley & Weaver 1995; Thielemann et al. 1996; Rauscher et al. 2002; Nomoto et al. 2006; Woosley & Heger 2007; Umeda & Nomoto 2008; Heger & Woosley 2010; Nomoto et al. 2013; Sukhbold et al. 2016; Chieffi & Limongi 2017; Nomoto 2017; Limongi & Chieffi 2018; Curtis et al. 2019; Ebinger et al. 2020; Ertl et al. 2020, for thermal bombs, piston, parametric neutrino heating explosions) with parameters fixed to reproduce observations of explosion energy and Ni yields. In addition, supernovae were suggested as the r-process sites where half of the elements beyond iron are produced (Burbidge et al. 1957; Woosley et al. 1994). With the improvement of simulations and neutrino treatment, it became clear that standard supernovae cannot produce elements beyond the second r-process peak, $A \sim 130$ (see Arcones & Thielemann 2013, for a review and references within). Current simulations show that the ejecta is often proton rich with some small, fast-expanding clumps of slightly neutron-rich material (Wanajo et al. 2011; Obergaullinger & Aloy 2020a). Therefore, elements between the iron group and the second r-process peak may be synthesized by a weak r-process under slightly neutron-rich conditions (Wanajo et al. (2011); Arcones & Bliss (2014); Bliss et al. (2020) and/or by the νp -process in proton-rich conditions (Fröhlich et al. 2006; Pruet et al. 2006; Wanajo 2006). In addition, observations of heavy r-process elements at low metallicities present a large scatter as a function of metallicity compared to iron group and alpha elements produced in core-collapse supernovae (see e.g., Sneden et al. 2008; Cowan et al. 2019, for recent reviews). This suggests that the r-process occurs only in rare events, and they may not happen in every core-collapse supernova. In the 1970s, the merger of a black hole and a neutron star was suggested as possible rare r-process event (Lattimer & Schramm 1974). In 2017, the production of r-process elements in neutron star mergers was confirmed by the observation of the kilonova light curve triggered by radioactive decay of neutron-rich nuclei after the gravitational wave detection of the merger GW170817 (Abbott et al. 2017b; Abbott et al. 2017a; Kasen et al. 2017; Pian et al. 2017; Smartt et al. 2017; Tanvir et al. 2017). However, such events have difficulties to explain the heavy elements observed in the oldest stars and the trend of Eu-over-Fe abundance ratios with metallicity (Côté et al. 2019). An additional r-process site has to exist at low metallicities and MR-SNe are a promising candidate.

LeBlanc & Wilson (1970) and later Cameron (2003) proposed MR-SNe as r-process site and Nishimura et al. (2006) presented the first successful results based on 2D adiabatic MHD simulations (i.e., ignoring the effects of neutrino cooling and heating). Similar results were found also with 3D simulations by Winteler et al. (2012), using a simplified and post-processed prescription of neutrino heating. For the rotation and magnetic fields, there are still many uncertainties in the progenitor models (e.g. Meynet et al. 2018). Based on simple neutrino treatment, Nishimura et al. (2015) have investigated the impact of different magnetic field strengths, and rotation rates on the nucleosynthesis. Nishimura et al. (2017) further improved the previous

study by considering the effects of the magnetic field enhancement as a result of the magnetorotational instability. Moreover, they also vary neutrino luminosities, which are not fully consistent but only a parameter in their models. In addition, Mösta et al. (2018) showed that the assumption of 2D may artificially support the production of heavy elements and that their 3D models needed even stronger magnetic fields to successfully produce heavy elements. They assumed that the neutron-rich material and thus the r-process occurs in the collimated ejecta and argue that this jet-like structure is not a robust 3D feature due to the kink instabilities. Also, a misalignment of the magnetic field with respect to the rotational axis can have an influence on the neutron-richness of the ejecta (reducing it), so that the r-process becomes weaker (Halevi & Mösta 2018). For the neutrinos, there are less uncertainties than for the magnetic field, but only recently it has been possible to perform MHD simulations with accurate neutrino transport, first in 2D (Obergaullinger et al. 2014a; Obergaullinger & Aloy 2017; Aloy & Obergaullinger 2020) and recently in 3D (Obergaullinger & Aloy 2020a,b; Kuroda et al. 2020).

Other potential r-process sites associated with MR-SNe are the accretion discs that form after the explosion surrounding a massive neutron star (magnetars) or a black hole (collapsars). Pioneering nucleosynthesis studies (Surman & McLaughlin 2004; McLaughlin & Surman 2005; Surman et al. 2006) have demonstrated that neutrinos will play a critical role reducing the neutron-richness of the ejecta and thus the possibilities for the r-process. Recent works are not conclusive (Miller et al. 2019; Siegel et al. 2019) and more work is required to understand the nucleosynthesis from supernova accretion discs.

In this paper, we have investigated the early explosive nucleosynthesis in MR-SNe based on the first 2D simulations that include a detailed neutrino transport treatment (Obergaullinger & Aloy 2017, 2020a,b; Aloy & Obergaullinger 2020). Advancing beyond state-of-the-art (see e.g., Nishimura et al. 2006; Winteler et al. 2012; Nishimura et al. 2015, 2017; Mösta et al. 2018), consisting on parametrizing rotation, magnetic field, and neutrinos, here we employ a self-consistent neutrino treatment. For the rotation and magnetic field, we start with the predictions from stellar evolution (Woosley & Heger 2006; Obergaullinger & Aloy 2017, 2020b) and vary them within the uncertainties that may result from stellar evolution and its mapping to multidimensional initial models for magnetorotational core collapse (Aloy & Obergaullinger 2020). In addition, to the original progenitor values, we use simulations with increased and decreased magnetic field and also increased rotation. A total of four models are analysed and found that the r-process can occur only in the model with moderately enhanced, topologically dipolar magnetic field. This explosion develops jets that become proton rich. Very neutron-rich matter is only promptly ejected and stays around the jet. We have also found that, during the late evolution (more than 1 s after bounce), the angular momentum redistribution can lead to a late ejection of neutron-rich material. In this model, we find a weak r-process producing elements up to the second r-process peak ($A \sim 130$).

This paper is structured as follows. In Sec. 2, we describe the magnetohydrodynamic models and the nuclear reaction network. The nucleosynthesis and dynamics of the ejecta are presented in Sec. 3. In Sec. 4, we briefly compare our results to different observations. Summary and conclusions are in Sec. 5.

2 METHODS

2.1 MHD simulations: code and input physics

We calculate the nucleosynthesis of four of the models whose dynamics has been described by [Obergaullinger & Aloy \(2017, 2020b\)](#). The simulations of the collapse and the explosion of the stellar cores were performed using the radiation-magnetohydrodynamics (MHD) code AENUS-ALCAR ([Just et al. 2015](#)). The dynamics of the gas and the magnetic field were modelled using the equations of special relativistic MHD. At high densities, $\rho > 6 \times 10^7 \text{ g cm}^{-3}$, the system is closed by the equation of state (EOS) of [Lattimer & Swesty \(1991\)](#) with an incompressibility of $K = 220 \text{ MeV}$. The EOS is tabulated on a 3D grid of density, temperature, and electron fraction. The range in Y_e is limited to a maximum of $Y_{e,\text{max}} = 0.56$. We encounter regions of our models in which the gas exceeds this maximum value and where we therefore rely on an extrapolation of the EOS in order to determine the thermodynamics of the gas. Below the density threshold, we use an EOS based on a gas of electrons, positrons, photons, and baryons ([Rampp & Janka 2002](#)). For the baryonic component, we used the so-called flashing scheme that assumes that matter is composed by a mixture of five nuclei, viz. protons, neutrons, α -particles, Si, and Ni nuclei. We accounted for the effects of general relativity in the gravitational field by using one of the post-Newtonian TOV potentials (version 'A'; see [Obergaullinger et al. 2006](#)) of [Marek et al. \(2006\)](#).

Neutrinos are treated in the spectral two-moment, or M1, framework derived by expanding the Boltzmann equation of radiative transfer into angular moments of the phase-space distribution function of the neutrinos. This expansion yields balance equations for the energy and momentum densities of the neutrinos. The system is closed by a local algebraic Eddington tensor. We evolve the neutrino moments in the frame comoving with the gas and include energy-bin coupling terms involving the fluid velocity and gravitational potential in the v/c -plus approximation of [Endeve et al. \(2012\)](#). Matter and neutrinos couple via the following reactions: emission and absorption of neutrinos by nucleons and nuclei, scattering of nucleons, nuclei, and electrons, electron-positron pair annihilation, and nucleonic bremsstrahlung. For more details, see [Obergaullinger et al. \(2014b\)](#) and [Obergaullinger et al. \(2018\)](#).

Our simulations are based on model 35OC for a star of an initial mass $M_{\text{ZAMS}} = 35 M_{\odot}$ from the stellar-evolution calculations by [Woosley & Heger \(2006\)](#). Rotation and magnetic fields were included in the spherically symmetric models following the recipe of [Spruit \(2002\)](#). Within the series of four models to which this progenitor belongs to, the mass-loss was a free parameter. As our reference model (35OC-RO), we selected the one with the second smallest mass-loss, which at collapse has a mass of $M = 28.1 M_{\odot}$ and an iron core of $M_{\text{Fe}} = 2.02 M_{\odot}$. It rotates differentially with an angular velocity $\Omega_c = 1.98 \text{ Hz}$ at the centre and $\Omega_{\text{Fe}} \approx 0.1 \text{ Hz}$ at the surface of the Fe core. The data contain the radial profiles of the poloidal and toroidal components of the magnetic field in the radiative layers. In convectively unstable layers, the field is set to zero by construction. With a field strength of $b^{\text{pol;tor}} \approx 1.7 \times 10^{10}; 1.7 \times 10^{11} \text{ G}$ for the poloidal and toroidal components at the centre of the core, the model possesses a relatively, though not extremely, high magnetization. We constructed the 2D distribution of the magnetic field from these radial profiles by assuming a sine dependence in θ (see [Aloy & Obergaullinger 2020](#)). The spherical grid used in our models consists of $(n_r, n_{\theta}) = (400, 128)$ zones, uniform in the polar angle θ and unevenly distributed in the radial direction (see [Obergaullinger & Aloy 2020b](#), for details).

2.2 Supernova models

The nucleosynthesis presented here is based on the four supernova models. We varied the original profiles of the rotational velocity and the magnetic field of model 35OC-RO to set-up the other three models. 35OC-Rw and 35OC-Rs are based on the same rotational profile, but replacing the magnetic field by an artificial distribution of poloidal and toroidal field following the prescription of [Suwa et al. \(2007\)](#). The normalisation of the field strengths is $b^{\text{pol}} = b^{\text{tor}} = 10^{10} \text{ G}$ for 35OC-Rw and $b^{\text{pol}} = b^{\text{tor}} = 10^{12} \text{ G}$ for 35OC-Rs, respectively. Model 35OC-RRw has an initial field that is six orders of magnitude weaker than that of 35OC-Rw and thus dynamically insignificant. It rotates 1.5 times faster than model 35OC-Rw.

The four models evolve in fairly different ways (see Table 1 for an overview of the models). Model 35OC-Rw develops a neutrino-driven explosion after about 400 ms post-bounce with a dynamically unimportant magnetic field at that time. Driven by strongly anisotropic neutrino fluxes, the explosion has the form of a relatively wide bipolar outflow. The shock wave reaches a polar radius of $R \approx 3 \times 10^4 \text{ km}$ at $t \approx 2 \text{ s}$. At that point, the ejecta contain an energy of $\approx 6 \times 10^{50} \text{ erg}$ and a mass of $\approx 0.2 M_{\odot}$. The final values are $R \approx 4.7 \times 10^4 \text{ km}$ for the maximum shock radius and $1.78 \times 10^{51} \text{ erg}$ and $\approx 0.321 M_{\odot}$ for the ejecta energy and mass, respectively. The proto-neutron star (PNS) grows in mass by accretion to a baryonic mass of $M \gtrsim M_{\text{bry}}^{\text{max}}$, with $M_{\text{bry}}^{\text{max}} = 2.45 M_{\odot}$ being the maximum cold, non-rotating PNS mass for our EOS. It develops a high rotational energy of up to $\mathcal{T} \approx 8 \times 10^{52} \text{ erg}$. The magnetic energy in and around the PNS grows continuously, but experiences a particularly strong increase after $t \sim 1.8 \text{ s}$. This growth causes a more efficient redistribution of angular momentum from the central regions to the outer layers of the PNS, where it is deposited (see [Aloy & Obergaullinger 2020](#), section 3.4). Consequently, growing centrifugal support leads to an expansion of the PNS at low latitudes. The increasingly oblate PNS sheds mass from its equatorial regions and thus generates a surrounding neutron-rich layer, with important consequences for the conditions of matter ejected.

Model 35OC-RO explodes earlier ($t \approx 178 \text{ ms}$) due to the strong magnetic forces that play an important role in accelerating the outflows. They furthermore lead to a stronger collimation than in model 35OC-Rw. The explosion is faster and more energetic, reaching the radius of $3 \times 10^4 \text{ km}$ and an energy of $6 \times 10^{50} \text{ erg}$ about 700 ms earlier than 35OC-Rw, whereas the evolution of the ejecta mass is very similar in both cases. By the end of the simulation, the shock expands to $R \approx 7.8 \times 10^4 \text{ km}$ and the ejecta have an energy of $1.78 \times 10^{51} \text{ erg}$ and a mass of $\approx 0.321 M_{\odot}$. The PNS is even more massive than in the previous model with $M \approx 2.7 M_{\odot}$ at $t \approx 2 \text{ s}$. Compared to model 35OC-Rw, the magnetic field in the PNS is stronger. Hence, efficient angular-momentum redistribution and the associated high axis ratio of the PNS develop earlier.

Model 35OC-Rs explodes almost immediately after core bounce. The explosion, driven entirely by the extremely strong magnetic fields, achieves a maximum radius of $3 \times 10^4 \text{ km}$ already at $t \approx 0.7 \text{ s}$. At that time, the energy and mass of the ejecta are $E \approx 3 \times 10^{51} \text{ erg}$ and $0.35 M_{\odot}$, i.e., they grow faster than in any other model. The PNS on the other hand has the lowest mass because the strong explosion shuts down accretion and magnetic stresses even drive the loss of the outer PNS layers. It reaches $M \approx 1.9 M_{\odot}$ at $t \approx 0.5 \text{ s}$ and afterwards tends to slowly lose mass. Without further accretion, the PNS also does not gain angular momentum, resulting in a comparably low rotational energy $\mathcal{T} \approx 2 \times 10^{52} \text{ erg}$ at $t \approx 0.7 \text{ s}$. Although the rotational energy is lower than in other models, the axis ratio of the PNS exceeds

Table 1. MR-SN models.

Name	Rotation ^a	Magnetic field ^b	t_{fin} ^c (s)	t_{exp} ^d (ms)	E_{exp} ^e (B)	M_{ej} ^f ($10^{-1} M_{\odot}$)	$\mathcal{T}/ \mathcal{W} $ ^g	\mathcal{B}/\mathcal{T} ^h	type ⁱ
35OC-RO	1.0	Or	2.5	178	1.78	3.21	0.028	0.092	MR
35OC-Rw	1.0	10	2.5	378	2.80	3.91	0.040	0.0089	ν - Ω
35OC-Rs	1.0	12	0.9	20	4.16	3.89	0.028	0.30	MR
35OC-RRw	1.5	$\text{Or} \times 10^{-6}$	1.6	343	0.209	0.345	0.063	2.9×10^{-5}	ν - Ω

^a Increase of the pre-collapse rotational velocity w.r.t. the original stellar evolution model.

^b Initial magnetic field: “Or” and “ $\text{Or} \times 10^{-6}$ ” denote the original field of the progenitor model ($b^{\text{pol;tor}} \approx 1.7 \times 10^{10}, 1.7 \times 10^{11}$ G) and the original field reduced by a uniform factor of 10^{-6} , respectively, and a number n indicates that the model was run using a normalization of both poloidal and toroidal components of 10^n G.

^c Time (post-bounce) of the last time-step of the simulations used for the nuclear network calculations (note that these models have been evolved for longer times in other publications, e.g. [Obergaulinger & Aloy \(2020b\)](#) and [Aloy & Obergaulinger \(2020\)](#)).

^d Time (post-bounce) at which an explosion is launched.

^e Diagnostic explosion energy at t_{fin} .

^f Ejected mass at t_{fin} .

^g Ratio of rotational to gravitational energy of the PNS at the time of explosion.

^h Ratio of magnetic to rotational energy of the PNS at the time of explosion.

ⁱ “Type” gives a brief indication of the explosion type: ν - Ω one strongly affected by rotation, MR a magnetorotational explosion.

theirs, because the extremely strong magnetic field accumulates a comparably large fraction of the angular momentum in the outer layers.

Model 35OC-RRw explodes at about the same time as 35OC-Rw, though less violently. At the end of the simulation ($t \approx 1.5$ s), the maximum shock radius is $R \approx 1.5 \times 10^4$ km, and the ejecta energy and mass are $E \approx 2 \times 10^{50}$ erg and $0.03 M_{\odot}$, respectively, i.e., considerably less than 35OC-Rw at the same time. The reason for this weaker explosion is that the high rotational energy ($\mathcal{T} \approx 1.2 \times 10^{53}$ erg at $t = 1.5$ s) reduces the accretion luminosity and, consequently, the neutrino heating rate. On the other hand, rotation allows for a high PNS mass of $M \approx 2.65 M_{\odot}$ and an exceptionally high axis ratio. A thorough overview of the post-bounce dynamics of all these models can be found in [Obergaulinger & Aloy \(2017, 2020b\)](#) and [Aloy & Obergaulinger \(2020\)](#).

2.3 Tracers and nucleosynthesis calculation

The evolution of the ejecta is followed by Lagrangian tracer particles that are set-up at the beginning of the simulations. Into each grid cell, we insert four tracer particles at random positions, corresponding to a total number of 204 800 tracers in each model. Each particle represents a fraction of one fourth of the total mass of the cell, $m_{\text{cell}} = \int_{\text{cell}} dV \rho$, where ρ is the local mass density. Consequently, the distribution of particle masses is non-uniform and biased towards regions of high density. This disparity is reduced by the logarithmic spacing of the radial grid as zones at higher radii have in general both larger volumes and lower densities.

The tracers record the evolution of density, temperature, radius, electron fraction, neutrino luminosities, and energies. This allows us to study the nucleosynthesis with the nuclear reaction network WINNET ([Winteler 2012; Winteler et al. 2012](#)) that contains 6545 nuclei up to $Z = 111$. The reaction rates are taken from the JINA ReacLib Database V2.0 ([Cyburt et al. 2010](#); accessed at 30/11/17) that is based on the finite-range droplet mass model ([Möller et al. 1995](#)). For nuclei with $Z \geq 83$, we include neutron captures and neutron-induced fission from [Panov et al. \(2010\)](#) and β -delayed fission probabilities from [Panov et al. \(2005\)](#). Neutrino reactions on nucleons are also included as in [Fröhlich et al. \(2006\)](#).

The nucleosynthesis calculations are performed for all tracers that are unbound at the end of the simulation. This set contains 6570, 7272, 17446, and 2218 particles for models 35OC-RO, 35OC-Rw,

35OC-Rs, and 35OC-RRw, respectively. We start the network when the temperature of the tracers drops below $T = 20$ GK. We assume nuclear statistical equilibrium (NSE) for $20 \text{ GK} > T > 7 \text{ GK}$ and evolve only the weak reactions and the corresponding Y_e variation¹. If the maximum temperature of a tracer is below 7 GK, we do not start from NSE but use the progenitor composition. For $T < 7 \text{ GK}$, the full network gives the detailed evolution of the abundances of each isotope. We run it until 1 Gyr, when most of the nuclei have decayed to stability. The tracers are extrapolated assuming an adiabatic expansion and density evolution as $\rho \propto t^{-3}$.

3 EJECTA DYNAMICS AND NUCLEOSYNTHESIS

The ejecta composition taking into account all tracers is presented in Fig. 1 for the models introduced in Sect. 2.2. The differences in the abundance patterns indicate that these models cover a wide range of nucleosynthesis conditions allowing to explore the impact of rotation, magnetic fields, and neutrinos. The models 35OC-RO and 35OC-RRw are close to typical supernova explosion and produce also “standard” nucleosynthesis, namely elements up to the iron group and a bit of lighter heavy elements around $A \sim 90$ (see e.g., [Harris et al. 2017; Eichler et al. 2018; Wanajo et al. 2018; Ebinger et al. 2020](#)). The model with strong magnetic fields (35OC-Rs) synthesizes elements up to the third r-process peak (see also [Nishimura et al. 2006; Winteler et al. 2012; Saruwatari et al. 2013; Nishimura et al. 2015, 2017; Halevi & Mösta 2018; Mösta et al. 2018](#)). The model 35OC-Rw is peculiar due to long-time evolution features that trigger the late ejection of neutron-rich material, see Sect. 3.2.

3.1 Nucleosynthesis patterns and hydrodynamical conditions

In order to understand the integrated abundances, we explore the hydrodynamical conditions of individual tracer particles and the corresponding nucleosynthesis contribution. The composition of every tracer particle is shown in the left-hand panels of Fig. 2. Groups of tracer particles with similar conditions lead also to similar abundance

¹ We observe deviations between the Y_e from the hydrodynamical simulations and the one calculated in the network. This can become significant and depends on the initial temperature. Starting at a high temperature of 20 GK reduces these discrepancies.

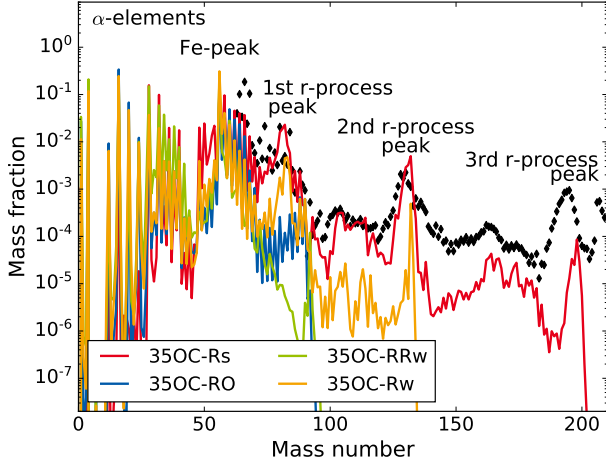


Figure 1. Integrated nucleosynthetic yields for the four models (see Sect. 2.2 and Table 1) corresponding to different rotation velocities and magnetic fields. The black diamonds show the solar r-process residual (Snedden et al. 2008), normalized to mass number $A = 88$.

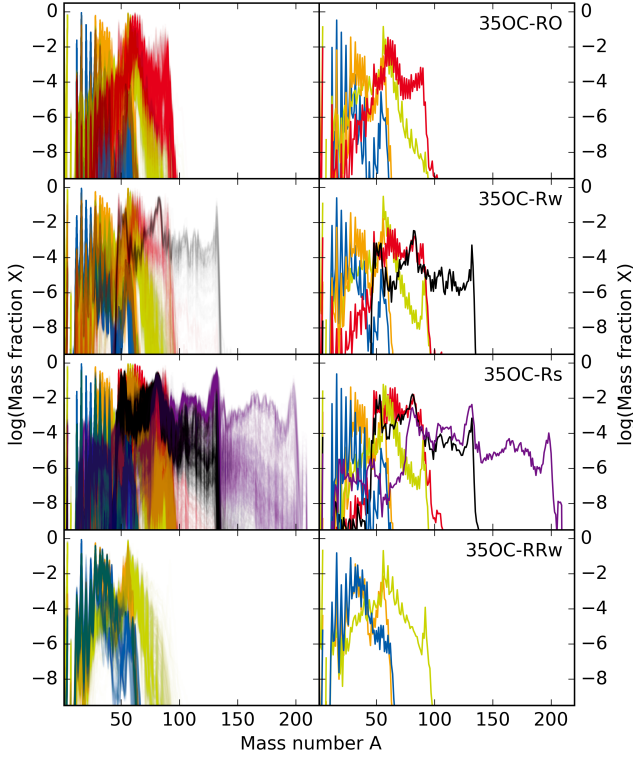


Figure 2. Composition of all ejected tracer particles, indicated by one color for each group, binned by a k-means clustering algorithm. Left-hand panels: Final mass fractions after decay for each individual tracer. Right-hand panels: Mass-weighted integrated composition separated into the different groups.

patterns. We have separated these groups with the help of a k-mean clustering algorithm (Lloyd 1982) for the abundances. The six groups are indicated by different colours and the average composition of each is shown in the right-hand panels of Fig. 2. Moreover, Figure 3 indicates the maximum density and temperature of each tracer showing the strong link between the tracer evolution and its nucleosynthesis.

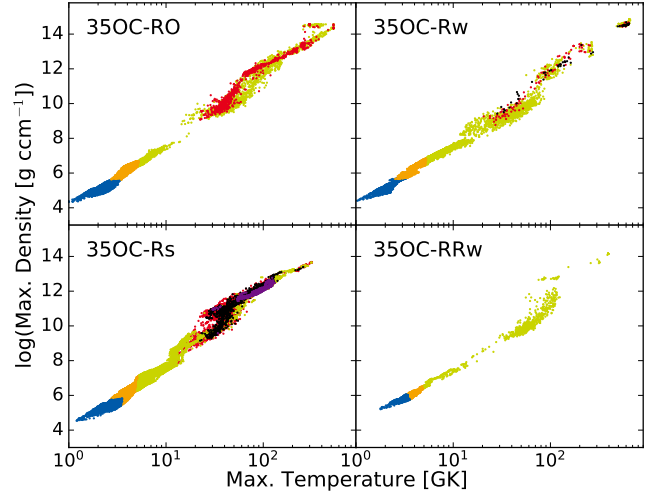


Figure 3. Maximum temperature and density of each tracer particle. The colours indicate nucleosynthetic groups as described in Sect. 3.1.

Every panel of this figure corresponds to one of the four models (see Table 1) and every dot to a tracer with the colours being the same as for the abundances in Fig. 2. The evolution relevant for nucleosynthesis can be explained by the nucleosynthesis parameters (Qian & Woosley 1996; Thompson et al. 2001) entropy and electron fraction shown in Fig. 4. Although the classification has been done based on abundance patterns, there is a clear dependence of the groups on the electron fraction. The histograms show the mass-weighted distributions of entropy and electron fraction. In all models, there is a peak around $Y_e = 0.5$. In addition to the entropy and electron fraction, the nucleosynthesis also depends on the expansion time-scale when the temperature drops down to around $T \approx 0.5$ MeV. Figure 5 shows the evolution of the radius for trajectories from different groups. There are three distinguished expansions: (1) trajectories that cross the shock and stays at large radii without approaching the neutron star, (2) trajectories that are promptly ejected from the outer layers of the PNS (bottom panel), and (3) trajectories that approach or even stay for some seconds close to the PNS and are ejected after being exposed to neutrinos.

In the following, we describe the six nucleosynthesis groups. The characteristics of a given group are the same for all models containing it, but only model 35OC-Rs contains all groups.

The α group (blue in Fig. 3) contains tracers that are located at large radii, which means that they encounter the shock at late times, just before the end of the simulation (see Fig. 5). Therefore, they do not change much in the course of their evolution and their maximum density and temperature do not exceed $\rho = 10^6 \text{ g cm}^{-3}$ and $T = 3 \text{ GK}$, respectively. Their electron fraction and final nuclear composition resembles the original progenitor values, i.e. mainly α -elements.

The α -Fe group (orange) corresponds to moderately heated progenitor material. The tracers of this group cross the shock at earlier times when the latter is more energetic. Therefore, the peak densities and temperatures are higher than for the α group ($\rho_{\text{peak}} \approx 10^7 \text{ g cm}^{-3}$ and $T_{\text{peak}} \approx 5 \text{ GK}$), leading to enhanced iron-group abundances due to explosive burning, alongside a considerable amount of α -elements.

These two groups (α and α -Fe) do not reach NSE conditions, and they are characterized by their peak quantities. This is visible by the clear and sharp separation of the groups in Fig. 3 compared to

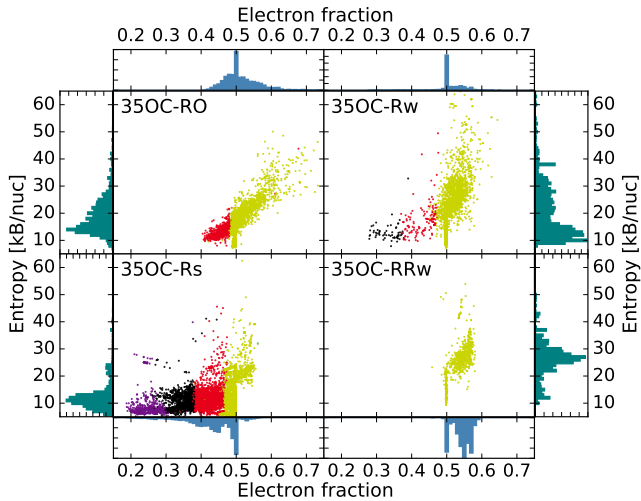


Figure 4. Electron fraction and entropy for each tracer at $T = 5.8$ GK together with their mass-weighted distributions at the outermost panels. Colours indicate the corresponding nucleosynthetic groups with the same color code as Fig. 2 and Fig. 3. Note that we only include tracer particles that reach a peak temperature of at least 5.8 GK here.

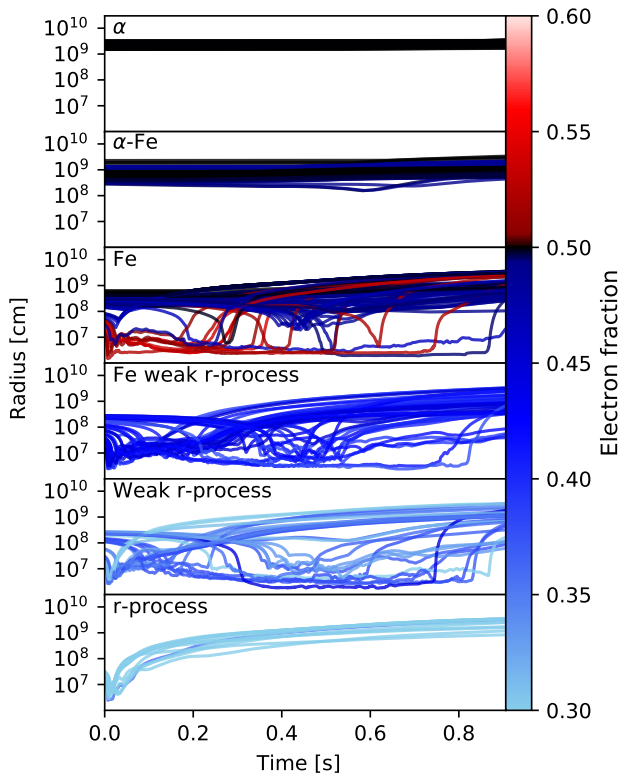


Figure 5. Radial evolution of tracers from different groups of model 35OC-Rs. The colours indicate the Y_e of the tracers at 5.8 GK or in the case of cooler trajectories the point of maximum temperature.

the other groups whose maximum values overlap. Therefore, for the groups described below, the maximum values are not determining the final abundances. Moreover, within a same group, i.e., same abundance pattern, there are tracers that seem to belong to different classes when viewed from a dynamic perspective. Especially in the case of the Fe, Fe-weak-r-process, and weak r-process groups, we can distinguish two subgroups of tracers defined by the time they start their outward propagation at high speeds (see Fig. 5).

One subgroup consists of tracers ejected shortly after they fall through the expanding shock wave (in the following denoted the *shock* subgroup) and another one contains tracers ejected after passing many dynamical time-scales in the vicinity of the PNS (*inner* subgroup).

The **Fe group** (green) clearly contains the two subgroups and the separation between both is visible in Fig. 3, especially for models 35OC-RO and 35OC-Rw for densities around 10^8 g cm^{-3} . The shock subgroup does not reach high values of the maximum temperature and density because matter does not approach the neutron star. This results in the electron fraction not changing much from the progenitor values and staying around $Y_e \sim 0.5$ or slightly below. In contrast, the tracers in the inner subgroup get close to the neutron star and are ejected later (Fig. 5). These tracers correspond to the Fe-group points with higher maximum densities and temperatures in Fig. 3 and with $Y_e > 0.5$ in Fig. 5 (the black- and red-coloured lines). In general, all tracers in both subgroups reach peak temperatures high enough to photo-disintegrate the progenitor composition and reach NSE. After NSE, their Y_e distribution extends from slightly neutron-rich to proton-rich conditions ($0.48 \leq Y_e \leq 0.6$; Fig. 4). Under these conditions, nuclear reactions favour the production of ^{56}Ni that later decays to ^{56}Fe , as well as lighter heavy elements up to Zr and Mo. This corresponds to typical nucleosynthesis found in neutrino-driven explosions without rotation and magnetic fields (e.g., Harris et al. 2017; Eichler et al. 2018; Wanajo et al. 2018). Notice that the proton-rich ejecta were not discussed in previous studies of MHD simulations because those did not include a detailed neutrino transport to accurately account for this.

The **Fe-weak-r-process group** (red) is slightly more neutron rich than the Fe-group with $0.38 \leq Y_e \leq 0.48$ (Fig. 4). Most of the tracers come close to the neutron star (inner group) and are ejected relatively fast, thus keeping the neutron-richness of the outer layers of the PNS star. Under such conditions the weak r-process produces lighter heavy elements from Sr to Ag. Final abundances reach $A \sim 100$ and are characterized by low abundances for alpha elements and high for iron group elements

The **weak r-process group** (black) is dominated by the inner subgroup of tracers with maximum temperatures of $T_{\text{max}} > 20$ GK and densities of $\rho_{\text{max}} = 10^9 \text{ g cm}^{-3}$. These values are similar to the ones of the Fe-weak-r-process group but Y_e is lower (Fig. 4) due to a faster expansion and thus shorter exposure to neutrinos in the expansion phase. These conditions favour the production of elements up to the second r-process peak around $A \sim 130$. This group is not a robust feature of all models. Instead, its presence depends on special conditions that are met only in two models, 35OC-Rs and, to a lesser degree, 35OC-Rw. In the former model, weak r-process tracers are ejected at all times, whereas in the latter only a unique transformation of the PNS causes them to appear at very late times (see Sect. 3.2).

The matter in the **r-process group** (purple) promptly and quickly accelerates from the neutron star surface and along the jets as indicated by the radius evolution shown in Fig. 5. This fast expansion prevents that the neutrinos transform neutrons into protons resulting in low electron fractions (Fig. 4). This group contains nuclei heavier than $A \geq 130$ and reaches the third r-process peak ($A \sim 195$). The

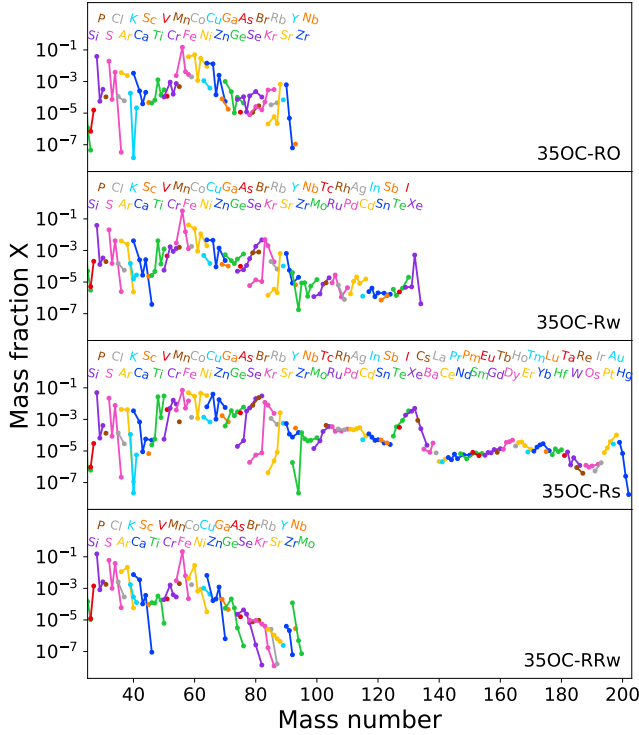


Figure 6. Mass fractions of individual isotopes for every model. Isotopes of a same elements are indicated by a given color and connected by a line. The element names are given at the top of each panel. Nuclei with mass fractions $\leq 10^{-8}$ are not included.

neutron-rich material of this group that is ejected very early along the jets shifts to the sides of the jet at later times. The late configuration consists of proton-rich jets surrounded by neutron-rich clumps where the r-process occurs.

3.2 Impact of rotation and the weak r-process

The effect of rotation can be investigated by comparing the two models with similar weak magnetic fields: 35OC-Rw and 35OC-RRw. Both models produce abundances for alpha elements and up to the iron group².

Model 35OC-RRw with strong rotation and weak magnetic field is characterized by only proton-rich ejecta in addition to the α and α -Fe groups. Rotation reduces the accretion and thus the accretion luminosity, and this makes the explosion slower and matter stays exposed to neutrinos for a longer time. The result is that the ejecta are proton rich as shown in Fig. 4. Here, we find typical nucleosynthesis produced by the νp -process when the matter flow runs on the proton-rich side of stability (Fröhlich et al. 2006; Pruet et al. 2006; Wanajo 2006). In addition, for conditions with $Y_e \sim 0.5$ or slightly proton- or neutron-rich, the flow goes along stability. The proton-rich conditions produce characteristic isotopic abundances including p-nuclei as shown in the bottom panel of Fig. 6, see Bliss et al. (2018); Eichler et al. (2018), and Wanajo et al. (2018) for more details about the nucleosynthesis in proton-rich supernova ejecta.

In the model with slower rotation (35OC-Rw), most of the matter

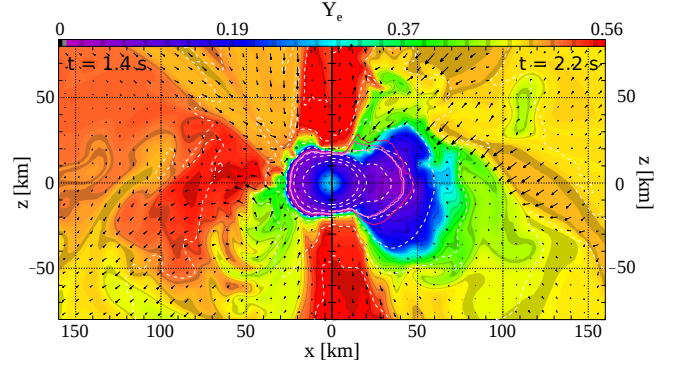


Figure 7. Electron fraction of model 35OC-Rw in a region around the PNS at $t \sim 1.4$ s (left-hand panel) and 2.2 s (right-hand panel). Contours of constant density (10^{14} , 10^{13} , ... g cm^{-3}) are indicated with the white, dashed lines. The pink contours correspond to the neutrinospheres.

is ejected with $Y_e \sim 0.5$ and a small amount is slightly neutron rich and the weak r-process produces the lighter heavy elements up to around Ag (see e.g., Bliss et al. 2017). In addition, there is a late matter ejection ($t \gtrsim 2$ s) with $Y_e \sim 0.3$. The sudden appearance of such a population of tracers is the consequence of a relatively abrupt change in the PNS structure that had occurred slightly earlier. Up to $t \sim 1.4$ s, the PNS is almost spherical with a decreasing radius and an aspect ratio close to unity despite having a very high rotational energy. Eventually, however, its magnetic field grows sufficiently to redistribute angular momentum to the outer layers. The excess centrifugal support causes these layers to expand and leads to a growth of the ratio between equatorial and polar radius beyond a value of two (Fig. 7). This expansion affects matter of very low Y_e (marked by the blue colours in the figure), some of which even ends up outside the neutrinospheres. The turbulent fluid flows in this region stochastically advect parcels of this very neutron-rich matter into the polar outflows. These fluid elements will be ejected at very high speeds and Y_e stays low (Fig. 4). We note that no similar transition from a spherical to an oblate PNS takes place in model 35OC-RO. There, the magnetic field is strong enough to cause a high aspect ratio already early on. Although we find neutron-rich matter outside the neutrinospheres also in this case, the amount is less and the structure of the PNS makes it less likely for this matter to enter the outflow, thus suppressing the weak r-process group.

3.3 Impact of the magnetic field and the r-process

Models 35OC-Rw, 35OC-RO, and 35OC-Rs show the impact of increasing magnetic field strengths on the abundances (Fig. 1). When increasing the magnetic field from model 35OC-Rw to model 35OC-RO, then elements around the second r-process peak are not produced anymore. This is related to the late evolution of model 35OC-Rw, discussed above. We note, however, that this non-monotonicity, caused by the presence or the absence of late neutron-rich fluid elements, only affects a small fraction of the ejecta. When these fluid elements are ignored, the distribution of the ejecta across Y_e behaves monotonically with initial magnetic field strength (Fig. 4).

Explosions with strong magnetic fields, like 35OC-Rs, have been suggested as a potential r-process site (e.g., Meier et al. 1976; Meyer 1994; Nishimura et al. 2006; Winteler et al. 2012; Nishimura et al. 2015, 2017; Mösta et al. 2018). The magnetic field produces a jet-like explosion and prompt ejection of neutron-rich material (Fig. 5).

² Note that the outer layers of the progenitor are not included here and they contribute to the alpha elements, see e.g., Eichler et al. (2018).

The formation and stability of the jets strongly depends on the magnetic field and is still under discussion (Mösta et al. 2014; Kuroda et al. 2020; Obergaulinger & Aloy 2020a). For strong magnetic fields, some neutron-rich matter is rapidly ejected by the magnetic pressure without major neutrino interactions with neutrons. Depending on whether the magnetic field or neutrinos dominate as ejection mechanism, we find a strong r-process or a weak r-process, respectively. This behaviour has been investigated in detail by, e.g. Nishimura et al. (2017) and Mösta et al. (2018) when they artificially varied the neutrino luminosity. Our neutrino treatment is self-consistent and the neutrino luminosity is not a free parameter.

In model 35OC-Rs, matter close to the neutron star and thus at small radii (Fig. 5) reaches high densities and temperatures (Fig. 2) and is promptly ejected. Due to the fast expansion, neutrinos are unable to convert too many neutrons into protons and the electron fraction stays low, $Y_e = 0.2 - 0.3$ (Fig. 4). Such conditions (i.e., fast expansion and low Y_e) allow for the r-process to produce elements up to the third r-process peak (Fig. 2).

In addition to the r-process, model 35OC-Rs ejects matter with different conditions leading to a large range of nucleosynthesis processes and products (Figs. 2 and 4). The jets are very proton-rich and contribute mainly to iron-group elements but also to heavier ones by the νp -process Pruet et al. (2006); Fröhlich et al. (2006), and Wanajo et al. (2018). Moreover, there is neutron-rich matter that is continuously ejected around the jets and produces elements up to the second r-process peak by a weak r-process. Remarkably, this neutron-rich matter comes from the PNS outer layers. It is extracted from there due to the mechanical action of the coherent, large-scale magnetic field in this model. As thoroughly discussed in Aloy & Obergaulinger (2020), this process is so strong that yields to a decrease in the PNS mass for $t \gtrsim 0.5$ s post-bounce.

4 OBSERVABLES

Here, we present a comparison of the nucleosynthesis produced in our models with observations, which focuses on three aspects: (1) the iron group element production that can be observed in supernova light curves, (2) heavy radioactive isotopes that may be visible by gamma- or X-rays, and (3) r-process elements compared to stellar elemental abundances. Table 2 provides the ejected mass of representative isotopes and elements for every model to get an overview. A full list of the synthesized isotopes is given in Appendix A in Tables A1, A2, A3, and A4.

4.1 Synthesis of Ni and Co.

The four models analysed give a good and reliable overview about the iron group elements produced in the first seconds of neutrino-driven and magneto-rotational-driven supernovae. Our calculations are the first ones based on detailed neutrino transport and long-time MHD simulations in 2D. We only investigate the nucleosynthesis of the innermost ejecta without including the outer layers of the star. Even if the simulations are followed for up to several seconds after the explosion, there is still matter that will be ejected later and that is hot enough to further contribute to the production of iron group nuclei. Therefore, the results discussed in the following show trends and lower limits for the mass ejected of given isotopes. The model 35OC-Rs provides a unique opportunity to study the early nucleosynthesis of a MR-SN and compare to observed hypernovae and long GRB-SNe. In addition, models 35OC-RO and 35OC-RRw are valuable

Table 2. Explosion energy and yields of selected isotopes and elements for different models.

	35OC-RO	35OC-Rw	35OC-Rs	35OC-RRw
$E_{\text{exp}} [B]$	1.78	2.8	4.16	0.21
^{26}Al	2.26 (-7)	1.94 (-6)	3.62 (-7)	4.33 (-7)
^{44}Ti	6.60 (-5)	1.34 (-4)	2.06 (-5)	1.16 (-5)
^{60}Fe	4.94 (-4)	1.55 (-4)	3.62 (-3)	1.69 (-7)
^{56}Ni	4.73 (-2)	1.21 (-1)	2.54 (-2)	7.32 (-3)
^{129}I	-	1.75 (-6)	6.93 (-4)	-
^{137}Cs	-	-	3.18 (-6)	-
^{247}Cm	-	-	2.30 (-12)	-
Mn	1.53 (-4)	6.23 (-4)	2.74 (-4)	6.87 (-4)
Zn	9.77 (-3)	4.23 (-3)	2.74 (-2)	2.81 (-3)
Sr	2.20 (-4)	2.56 (-4)	1.03 (-3)	1.65 (-6)
Y	2.22 (-5)	4.05 (-5)	2.23 (-4)	8.42 (-8)
Zr	2.01 (-4)	2.84 (-4)	3.45 (-4)	1.29 (-7)
Ba	-	2.84 (-10)	2.07 (-5)	-
Pr	-	-	7.94 (-7)	-
Nd	-	-	1.07 (-5)	-
Eu	-	-	5.19 (-6)	-
Dy	-	-	5.29 (-5)	-
Pt	-	-	6.39 (-5)	-
Au	-	-	1.06 (-5)	-

Note: Yields in M_{\odot} using the notation $A(B)$ for $A \times 10^B$. Radioactive isotope yields are given as maximum synthesized value. Note that ^{26}Al and ^{60}Fe are also synthesized during stellar evolution (e.g., Limongi & Chieffi 2006) and the progenitor contribution is not included here.

examples for standard neutrino-driven supernova nucleosynthesis including rotation and magnetic fields in the computational set-up.

The values that we find for ^{56}Ni range from $7.3 \times 10^{-3} M_{\odot}$ for the fast-rotating and weakly exploding model (35OC-RRw) to $1.2 \times 10^{-1} M_{\odot}$ for model 35OC-Rw. The amount of ^{56}Ni and explosion energy correlates for the three models without strong magnetic field (see Table 2). Model 35OC-Rs, with strong magnetic field, has significantly larger explosion energy while the ejected ^{56}Ni mass is still low, although this may increase as nucleosynthesis is still going on at the end of the simulation. In any case, it may be unlikely that the amount of Ni still increases from $2.5 \times 10^{-2} M_{\odot}$ to larger than $\sim 0.3 M_{\odot}$ as predicted by hypernova observations (see Iwamoto et al. 1998; Nakamura et al. 2001; Mazzali et al. 2003; Nomoto et al. 2006 and references therein). The explosion energy of this model is also below the typical hypernova energy (> 10 B) but it may still increase enough to become a low-energy hypernova. In general, our models produce explosion energies and ^{56}Ni masses that are similar to values from observations (e.g., for SN1987A $M(^{56}\text{Ni}) \approx 7 \times 10^{-2} M_{\odot}$ from Seitenzahl et al. 2014). Another radioactive isotope observed in supernovae remnants is ^{44}Ti with for example $M(^{44}\text{Ti}) \approx 5.5 \times 10^{-5} M_{\odot}$ for SN1987A (Seitenzahl et al. 2014) and $M(^{44}\text{Ti}) \approx 1.3 \times 10^{-4} M_{\odot}$ for Cas A (Wang & Li 2016). Our yields are around these estimates, although the exact observed value may be still uncertain (see Grebenev et al. 2012; Seitenzahl et al. 2014; Weinberger et al. 2020) or the individual values of the compared stars may be exceptional (which may be the case in SN1987A; Podsiadlowski 1992).

4.2 Radioactive isotopes

The decay of radioactive isotopes produced during the supernova explosion can be observed by their gamma- and X-rays. This is a direct observation of supernovae and stellar nucleosynthesis as it has been done for ^{44}Ti , ^{26}Al , ^{60}Fe , and more (see Diehl & Timmes 1998;

Diehl et al. 2007, for reviews). Heavy radioactive isotopes have not been observed yet although this may become possible as suggested by previous studies (Qian et al. 1998; Ripley et al. 2014; Korobkin et al. 2020).

Here, we briefly show the production of some radioactive isotopes in our models and their potential detection. The flux for a given ejecta composition is (Qian et al. 1998)

$$F_\gamma = \frac{N_A}{4\pi d^2} \frac{M_x}{A} \frac{I_\gamma}{\bar{\tau}}, \quad (1)$$

where N_A is the Avogadro's number, d the distance to the remnant, M_x the mass of nucleus x , I_γ the number of photons per energy emitted, and $\bar{\tau} = T_{1/2}/\ln(2)$ the lifetime of the investigated nucleus. For I_γ we take values obtained from the Lund/LBNL Nuclear Data Search³, whereas we use lifetimes from Nuclear Wallet Cards (Tuli 2011). Notice that our calculation is only an estimate, the obtained spectrum contains only emission lines, no continuum emission (e.g., by bound-free or free-free interactions), and no absorption. Furthermore, we did not take any line-broadening effect into account and when observed with a real telescope, the emission lines will have a distribution with finite width and therefore a lower maximum flux.

We investigate model 35OC-Rs and take only one representative trajectory of each nucleosynthetic group weighted by the mass of the corresponding group. Several studies and observations are available for iron group (e.g., ^{44}Ti) and lighter nuclei (^{26}Al , ^{60}Fe). Here we find also those light isotopes (see Table 2) and go beyond by looking at the emission from heavy r-process nuclei.

The time when to detect the gamma- and X-rays is critical. At early times after the event, the total flux will be higher. Due to the still high velocities of the ejecta in addition to large and slowly decreasing opacities, the detection will, however, be challenging. Nevertheless, there are studies that identified peculiar features of individual emission lines in the afterglow of GRBs (Margutti et al. 2008; Campana et al. 2016). Remarkably, Margutti et al. (2008) found an emission line around $E_\gamma \sim 7.85$ keV. This coincides with the emission lines of Ni and Cr radioactive isotopes at around these energies at early times (Fig. 8). Similarly, the spectrum shows a feature around $E_\gamma \sim 0.5$ keV, which again agrees with emission lines of iron group nuclei in the spectrum. Heavier r-process elements lead to lower fluxes than iron group nuclei that dominate the spectrum. Therefore, it does not seem likely to make a direct detection of the r-process in the spectrum at early times.

Another possibility for a detection can be achieved by looking at later times at SN remnants (Qian et al. 1998; Ripley et al. 2014), where short-lived radioactive isotopes have already decayed. In the remnants of SN1987A and Cassiopeia A, ^{44}Ti emission lines were detected around $E_\gamma \sim 68$ and ~ 78 keV (Grebenev et al. 2012; Grefenstette et al. 2014). These emission lines are also visible in the lower panels of Fig. 8. When focusing on r-process elements, there exists emission lines of ^{137}Cs , ^{155}Eu , ^{194}Ir , and ^{194}Os (lower panels of Fig. 8). The feature of ^{137}Cs maintains a relatively high flux even after an extreme time of 100 yr.

Fig. 9 shows the time and distance for known supernova remnants together with the expected flux from the decay of ^{137}Cs from a MR-SN at given distance and age. As indicated by the dashed line, only remnants within ~ 3 kpc may provide a significant signal. Whether these features can be observed with upcoming detectors is beyond the scope of our work.

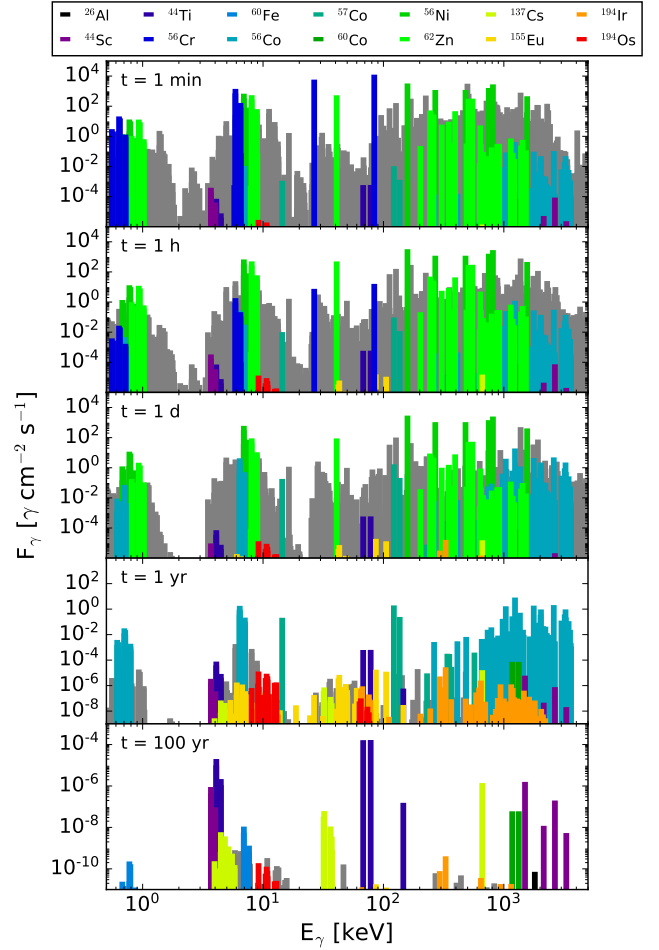


Figure 8. Flux at 1 kpc for different emission lines of model 35OC-Rs. Each panel corresponds to different times.

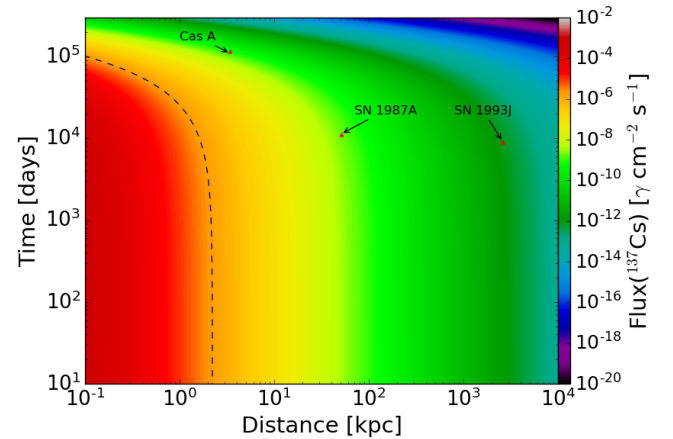


Figure 9. Flux of the ^{137}Cs gamma-ray line at $E_\gamma = 661.7$ keV. Shown is time versus distance of the source. The dashed line indicates a constant flux of $2 \times 10^{-6} \gamma \text{ cm}^{-2} \text{ s}^{-1}$, which is a flux that could be detected by gamma-ray telescopes as AMEGO (Rando 2017) or e-ASTROGAM (De Angelis et al. 2017) at $E_\gamma \approx 1$ MeV. Data for Cas A were taken from Ferrand & Safi-Harb (2012); Green (2009), for SN1987A from Panagia (2003), and for SN 1993J from Freedman et al. (1994).

³ <http://nucleardata.nuclear.lu.se/toi/>, the database was compiled by S.Y.F. Chu, L.P. Ekström and R.B. Firestone.

4.3 r-process and UMP stars

Ultra-metal-poor (UMP) stars belong to the oldest stars and thus they provide a unique possibility to study the nucleosynthesis from MR-SNe produced from sub-solar metallicity stellar progenitors and validate our models against observations (see also [Nishimura et al. 2017](#)). The elemental abundances observed in the atmosphere of such old stars come from few previous nucleosynthesis events. We compare observed abundances to our models in Fig. 10. Usually there are two types of abundance patterns with high and low enrichment of the elements between second and third r-process peaks (see e.g., [Qian & Wasserburg 2001, 2007, 2008](#); [Hansen et al. 2014](#)). Most of the stars with high enrichment of heavy r-process elements present a robust pattern for those, meaning that the relative abundances among elements are very similar among different stars and also follow the solar r-process (see e.g., [Snedden et al. 2008](#)). These stars are sometimes called “Snedden-like” stars. For the lighter heavy elements below the second peak, even in Sneden-like stars, there is more variability or less robustness in the patterns. In addition, there are many different patterns for stars with low enrichment of heavy r-process elements ([McWilliam 1998](#); [Aoki et al. 2005](#); [Honda et al. 2006](#); [Roederer et al. 2010](#)). These are called “Honda-like” stars.

In Figure 10, we show how our models can explain different observational features. Models 35OC-RO and 35OC-RRw contribute to the lighter heavy elements as expected from standard supernova nucleosynthesis ([Harris et al. 2017](#); [Bliss et al. 2018](#); [Eichler et al. 2018](#); [Wanajo et al. 2018](#)). This supernova contribution to the lighter heavy elements can give an explanation to the variability of the abundance patterns for those elements ([Qian & Wasserburg 2001](#); [Snedden et al. 2008](#); [Hansen et al. 2014](#)). Model 35OC-RW, with its peculiar late evolution, reaches the second r-process peak. This model can provide some hints to the weak r-process production of elements beyond Sr, Y, Zr but still below the second peak. Finally, the model with strong magnetic field (35OC-Rs) produces the heavy r-process elements following a Honda-like pattern, rather than a robust, Sneden-like pattern. In summary, MR-SNe with variations in the rotation and magnetic field can explain the broad variability in abundance patterns found in UMP stars. Still further investigations and models are necessary to understand whether some of these supernovae can also produce a robust r-process.

5 CONCLUSIONS

We have presented the first nucleosynthesis yields from MR-SNe that are based on 2D simulations including detailed neutrino transport. This is critical to consistently account for the neutrino-driven ejecta and to be able to compare to the magneto-rotational ejecta. Our study is based on four models from [Obergaullinger & Aloy \(2017, 2020b\)](#) with different rotation and magnetic fields. The nucleosynthesis obtained from these models can be classified into six groups depending on the abundance pattern. The model with strong magnetic field has the richest nucleosynthesis from shocked heated to r-process including also proton-rich outflows.

In all models, there is matter ejected after crossing the shock, without being accreted into the PNS, and the composition is dominated by alpha particles and iron-group elements. This matter corresponds to our α and α -Fe groups. We also find a transition group with some tracers accreted down to the PNS before being ejected. These tracers correspond to the Fe-group and change from very neutron-rich when they start at the PNS surface to slightly neutron-rich or even proton-rich due to neutrinos. Similar but a bit more neutron-rich is

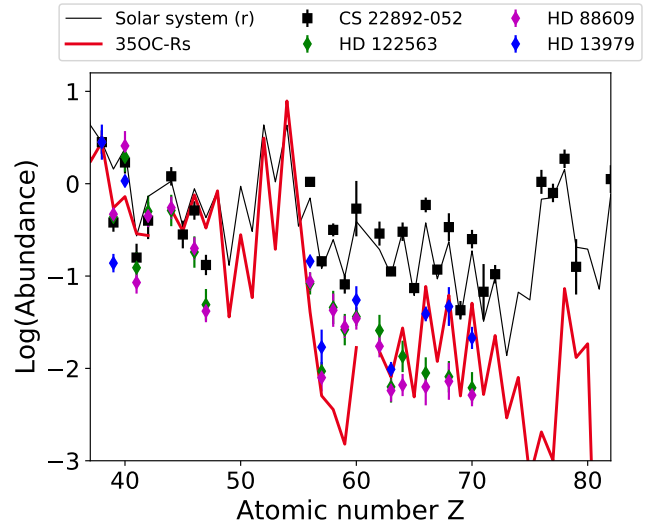


Figure 10. Comparison of the final abundances to the r-process enriched star CS 22892-052 ([Snedden et al. 1996](#)), HD 122563 ([Honda et al. 2006](#)), HD 88609 ([Honda et al. 2007](#)), and HD 13979 ([Roederer et al. 2014](#)). We have normalized all abundances to strontium ($Z = 38$) of model 35OC-Rs.

the Fe-weak-r-process group, where lighter heavy elements are synthesized. Finally, we find two r-process groups: the weak-r-process group that is present only in two models and the r-process group characteristic of the magneto-rotational ejecta of the model with strong magnetic fields. While the nucleosynthesis of the first groups, α to Fe and even Fe-weak-r-process, is typical from neutrino-driven ejecta from standard supernovae, the r-process groups are characteristics of MR-SNe.

In the model with weak magnetic field and the original progenitor rotation, there is a late ejection of neutron-rich material at around $t \approx 1.2$ s. This enables the weak r-process to produce elements up to the second peak. The late ejection is due to angular momentum redistribution by the magnetic field that leads to a sudden deformation of the neutron star. The change in the neutron star allows some neutron-rich material to enter outflow regions. We conclude that long-time simulations of MR-SNe are critical to account for the total nucleosynthesis (see also [Aloy & Obergaullinger 2020](#)).

The model with strong magnetic field, in agreement with previous studies (e.g., [Nishimura et al. 2006](#); [Winteler et al. 2012](#); [Saruwatari et al. 2013](#); [Nishimura et al. 2015, 2017](#); [Halevi & Mösta 2018](#); [Mösta et al. 2018](#)), ejects promptly neutron-rich matter. We again stress that, even more than the strength of the (poloidal) magnetic field, its large-scale, dipolar morphology is the key to produce MR-SNe ([Bugli et al. 2020](#); [Aloy & Obergaullinger 2020](#)). This very early ejection of matter prevents that neutrinos change neutrons into protons and thus the r-process successfully produces heavy elements up to the third peak. This model (35OC-Rs) develops into a jet-like explosion with proton-rich jets surrounded by the early-ejected, neutron-rich material. The r-process pattern from this model does not agree with the solar r-process. This is partially due to the uncertainties in the nuclear physics input (see [Cowan et al. 2019](#); [Horowitz et al. 2019](#) for recent reviews) and also may indicate that the r-process in our Sun does not come only from MR-SNe but also from neutron star mergers ([Côté et al. 2019](#)). Moreover, MR-SNe were probably more frequent in the early Galaxy because low metallicity stars have lower mass-loss rates and can become fast rotators ([Brott et al. 2011](#)). MR-SNe can also explain the missing contribution to the europium

production in the early Galaxy when one assumes only mergers as r-process site (Côté et al. 2019). We have compared the r-process pattern to observed elemental abundances in old stars and found that our results are within the observed abundances of what is called Honda-like stars, i.e., stars with low enrichment of heavy r-process beyond the second peak.

We find a correlation between the explosion energy and the ^{56}Ni production for the three models without strong magnetic field. The latter has higher explosion energy than the other models and relative low ^{56}Ni , far from what is needed to explain hypernovae. However, our yields are lower limits as we do not consider the matter that becomes unbound at late times or from the progenitor. Even if these two contributions were added, we do not expect to reach the ^{56}Ni that is needed to explain hypernovae from the explosion. Yet, matter ejected from the disc, which may form at late times, could provide the missing ^{56}Ni . In general, the amount of ^{56}Ni and ^{44}Ti produced by our models is close to observed values in supernova remnants (e.g. Seitenzahl et al. 2014; Wang & Li 2016). Moreover, we have discussed the possibility of observing the gamma- or X-rays from the radioactive decay of heavy elements produced in MR-SN. We have found that ^{137}Cs may be observed for a MR-SN within 3 kpc.

MR-SNe show a huge nucleosynthesis richness and may be critical to explain the early r-process in our Galaxy. Our study demonstrates that only with MHD simulations including detailed neutrino transport, one can accurately calculate the complete nucleosynthesis. However, further simulations are needed to investigate the impact of 3D and different configurations of the magnetic field and improve our understanding of the role of MR-SNe in the origin of heavy elements in the universe.

ACKNOWLEDGEMENTS

We thank Julia Bliss, Takami Kuroda, Dirk Martin, and Friedel Thielemann for useful discussions. This research was supported by the ERC Starting Grant EUROPIUM-677912, Deutsche Forschungsgemeinschaft through SFB 1245, Helmholtz Forschungsakademie Hessen für FAIR, and by the Helmholtz-University Young Investigator grant No. VH-NG-825. MO acknowledges support from the Ministerio de Ciencia e Innovación via the Ramón y Cajal program (RYC2018-024938-I). MAA and MO acknowledge the support by the Ministerio de Ciencia, Innovación y Universidades (PGC2018-095984-B-I00) and the Generalitat Valenciana (PROM-ETEU/2019/071). This work has benefited from the COST Actions “ChETEC” (CA16117) and “PHAROS” (CA16214), supported by COST (European Cooperation in Science and Technology). Nucleosynthesis computations were performed on the Lichtenberg High Performance Computer (TU Darmstadt). MAA and MO thankfully acknowledge the computer resources and the technical support provided by the grants AECT-2017-2-0006, AECT-2017-3-0007, AECT-2018-1-0010, AECT-2018-2-0003, AECT-2018-3-0010, and AECT-2019-1-0009 of the Spanish Supercomputing Network on clusters *Pirineus* of the Consorci de Serveis Universitaris de Catalunya (CSUC), *Picasso* of the Universidad de Málaga, and *MareNostrum* of the Barcelona Supercomputing Centre - Centro Nacional de Supercomputación, respectively, and on the clusters *Tirant* and *Lluïsvives* of the Servei d’Informàtica of the University of Valencia (financed by the FEDER funds for Scientific Infrastructures; IDIFEDER-2018-063).

DATA AVAILABILITY

Ten representative tracer particles of every nucleosynthesis group of Model 35OC-Rs can be found at <https://theorie.ikp.physik.tu-darmstadt.de/astro/resources.php> and https://github.com/nuc-astro/RepresentativeTrajectories_MagnetoRotationalSupernova. The integrated nucleosynthetic yields of the innermost part of the ejecta are given in the appendix.

REFERENCES

- Abbott B. P., et al., 2017a, *Phys. Rev. Lett.*, 119, 161101
 Abbott B. P., et al., 2017b, *ApJ*, 848, L12
 Aloy M.-Á., Obergaulinger M., 2020, arXiv e-prints, p. arXiv:2008.03779
 Aoki W., et al., 2005, *ApJ*, 632, 611
 Arcones A., Bliss J., 2014, *Journal of Physics G Nuclear Physics*, 41, 044005
 Arcones A., Thielemann F. K., 2013, *Journal of Physics G Nuclear Physics*, 40, 013201
 Bliss J., Arcones A., Montes F., Pereira J., 2017, *Journal of Physics G Nuclear Physics*, 44, 054003
 Bliss J., Arcones A., Qian Y. Z., 2018, *ApJ*, 866, 105
 Bliss J., Arcones A., Montes F., Pereira J., 2020, *Phys. Rev. C*, 101, 055807
 Brott I., et al., 2011, *A&A*, 530, A115
 Bugli M., Guilet J., Obergaulinger M., Cerdá-Durán P., Aloy M. A., 2020, *MNRAS*, 492, 58
 Burbidge E. M., Burbidge G. R., Fowler W. A., Hoyle F., 1957, *Reviews of Modern Physics*, 29, 547
 Cameron A. G. W., 2003, *ApJ*, 587, 327
 Campana S., et al., 2016, *A&A*, 592, A85
 Cano Z., Wang S.-Q., Dai Z.-G., Wu X.-F., 2017, *Advances in Astronomy*, 2017, 8929054
 Chieffi A., Limongi M., 2017, *ApJ*, 836, 79
 Côté B., et al., 2019, *ApJ*, 875, 106
 Cowan J. J., Sneden C., Lawler J. E., Aprahamian A., Wiescher M., Langanke K., Martínez-Pinedo G., Thielemann F.-K., 2019, arXiv e-prints, p. arXiv:1901.01410
 Curtis S., Ebinger K., Fröhlich C., Hempel M., Perego A., Liebendörfer M., Thielemann F.-K., 2019, *ApJ*, 870, 2
 Cyburt R. H., et al., 2010, *ApJS*, 189, 240
 De Angelis A., et al., 2017, *Experimental Astronomy*, 44, 25
 Dessart L., Burrows A., Livne E., Ott C. D., 2008, *ApJ*, 673, L43
 Dessart L., Hillier D. J., Waldman R., Livne E., Blondin S., 2012, *MNRAS*, 426, L76
 Diehl R., Timmes F. X., 1998, *PASP*, 110, 637
 Diehl R., Hartmann D. H., Prantzos N., 2007, *Meteoritics and Planetary Science*, 42, 1145
 Duncan R. C., Thompson C., 1992, *ApJ*, 392, L9
 Ebinger K., Curtis S., Ghosh S., Fröhlich C., Hempel M., Perego A., Liebendörfer M., Thielemann F.-K., 2020, *ApJ*, 888, 91
 Eichler M., et al., 2018, *Journal of Physics G Nuclear Physics*, 45, 014001
 Endeve E., Cardall C. Y., Mezzacappa A., 2012, preprint, (arXiv:1212.4064)
 Ertl T., Woosley S. E., Sukhbold T., Janka H. T., 2020, *ApJ*, 890, 51
 Ferrand G., Safi-Harb S., 2012, *Advances in Space Research*, 49, 1313
 Freedman W. L., et al., 1994, *ApJ*, 427, 628
 Fröhlich C., Martínez-Pinedo G., Liebendörfer M., Thielemann F.-K., Bravo E., Hix W. R., Langanke K., Zinner N. T., 2006, *Physical Review Letters*, 96, 142502
 Grebenev S. A., Lutovinov A. A., Tsygankov S. S., Winkler C., 2012, *Nature*, 490, 373
 Green D. A., 2009, *Bulletin of the Astronomical Society of India*, 37, 45
 Grefenstette B. W., et al., 2014, *Nature*, 506, 339
 Halevi G., Mösta P., 2018, *MNRAS*, 477, 2366
 Hansen C. J., Montes F., Arcones A., 2014, *ApJ*, 797, 123
 Harris J. A., Hix W. R., Chertkow M. A., Lee C. T., Lentz E. J., Messer O. E. B., 2017, *ApJ*, 843, 2
 Heger A., Woosley S. E., 2010, *ApJ*, 724, 341

- Hillebrandt W., Takahashi K., Kodama T., 1976, *A&A*, **52**, 63
- Honda S., Aoki W., Ishimaru Y., Wanajo S., Ryan S. G., 2006, *ApJ*, **643**, 1180
- Honda S., Aoki W., Ishimaru Y., Wanajo S., 2007, *ApJ*, **666**, 1189
- Horowitz C. J., et al., 2019, *Journal of Physics G Nuclear Physics*, **46**, 083001
- Iwamoto K., et al., 1998, *Nature*, **395**, 672
- Janka H.-T., Melson T., Summa A., 2016, *Annual Review of Nuclear and Particle Science*, **66**, 341
- Just O., Obergaulinger M., Janka H.-T., 2015, *MNRAS*, **453**, 3386
- Kasen D., Metzger B., Barnes J., Quataert E., Ramirez-Ruiz E., 2017, *Nature*, **551**, 80
- Kaspi V., Beloborodov A., 2017, *Annual Review of Astronomy and Astrophysics*, **55**, null
- Korobkin O., et al., 2020, *ApJ*, **889**, 168
- Kotake K., Sumiyoshi K., Yamada S., Takiwaki T., Kuroda T., Suwa Y., Nagakura H., 2012, *Progress of Theoretical and Experimental Physics*, **2012**, 01A301
- Kuroda T., Arcones A., Takiwaki T., Kotake K., 2020, *ApJ*, **896**, 102
- Lattimer J. M., Schramm D. N., 1974, *ApJ*, **192**, L145
- Lattimer J. M., Swesty F. D., 1991, *Nuclear Physics A*, **535**, 331
- LeBlanc J. M., Wilson J. R., 1970, *ApJ*, **161**, 541
- Limongi M., Chieffi A., 2006, *ApJ*, **647**, 483
- Limongi M., Chieffi A., 2018, *ApJS*, **237**, 13
- Lloyd S. P., 1982, *IEEE Transactions on Information Theory*, **28**, 129
- Maeda K., Nomoto K., 2003, *ApJ*, **598**, 1163
- Marek A., Dimmelmeier H., Janka H.-T., Müller E., Buras R., 2006, *A&A*, **445**, 273
- Margutti R., et al., 2008, *A&A*, **480**, 677
- Mazzali P. A., et al., 2003, *ApJ*, **599**, L95
- Mazzali P. A., McFadyen A. I., Woosley S. E., Pian E., Tanaka M., 2014, *MNRAS*, **443**, 67
- McLaughlin G. C., Surman R., 2005, *Nuclear Phys. A*, **758**, 189
- McWilliam A., 1998, *AJ*, **115**, 1640
- Meier D. L., Epstein R. I., Arnett W. D., Schramm D. N., 1976, *ApJ*, **204**, 869
- Metzger B. D., Giannios D., Thompson T. A., Bucciantini N., Quataert E., 2011, *MNRAS*, **413**, 2031
- Metzger B. D., Margalit B., Kasen D., Quataert E., 2015, *MNRAS*, **454**, 3311
- Metzger B. D., Beniamini P., Giannios D., 2018, *ApJ*, **857**, 95
- Meyer B. S., 1994, *ARA&A*, **32**, 153
- Meynet G., Choplin A., Ekström S., Georgy C., 2018, in Chiappini C., Minchev I., Starenburg E., Valentini M., eds, *Proceedings of IAU Symposium 334 Vol. 334, Rediscovering Our Galaxy*. pp 170–177 ([arXiv:1711.04554](https://arxiv.org/abs/1711.04554)), doi:10.1017/S1743921317010808
- Miller J. M., Sprouse T. M., Fryer C. L., Ryan B. R., Dolence J. C., Mumpower M. R., Surman R., 2019, *arXiv e-prints*, p. [arXiv:1912.03378](https://arxiv.org/abs/1912.03378)
- Möller P., Nix J. R., Myers W. D., Swiatecki W. J., 1995, *Atomic Data and Nuclear Data Tables*, **59**, 185
- Moriya T. J., Sorokina E. I., Chevalier R. A., 2018, *Space Sci. Rev.*, **214**, 59
- Mösta P., et al., 2014, *ApJ*, **785**, L29
- Mösta P., Roberts L. F., Halevi G., Ott C. D., Lippuner J., Haas R., Schnetter E., 2018, *ApJ*, **864**, 171
- Müller B., 2020, *Living Reviews in Computational Astrophysics*, **6**, 3
- Nakamura T., Mazzali P. A., Nomoto K., Iwamoto K., 2001, *ApJ*, **550**, 991
- Nishimura S., Kotake K., Hashimoto M.-a., Yamada S., Nishimura N., Fujimoto S., Sato K., 2006, *ApJ*, **642**, 410
- Nishimura N., Takiwaki T., Thielemann F.-K., 2015, *ApJ*, **810**, 109
- Nishimura N., Sawai H., Takiwaki T., Yamada S., Thielemann F.-K., 2017, *ApJ*, **836**, L21
- Nomoto K., 2017, *Nucleosynthesis in Hypernovae Associated with Gamma-Ray Bursts*. Springer International Publishing, Cham, pp 1931–1954, doi:10.1007/978-3-319-21846-5_86, https://doi.org/10.1007/978-3-319-21846-5_86
- Nomoto K., Tominaga N., Umeda H., Kobayashi C., Maeda K., 2006, *Nuclear Physics A*, **777**, 424
- Nomoto K., Kobayashi C., Tominaga N., 2013, *ARA&A*, **51**, 457
- Obergaulinger M., Aloy M. Á., 2017, *MNRAS*, **469**, L43
- Obergaulinger M., Aloy M. Á., 2020a, *arXiv e-prints*, p. [arXiv:2008.07205](https://arxiv.org/abs/2008.07205)
- Obergaulinger M., Aloy M. Á., 2020b, *MNRAS*, **492**, 4613
- Obergaulinger M., Aloy M. A., Dimmelmeier H., Müller E., 2006, *A&A*, **457**, 209
- Obergaulinger M., Cerdá-Durán P., Müller E., Aloy M. A., 2009, *A&A*, **498**, 241
- Obergaulinger M., Janka H. T., Aloy M. A., 2014a, *MNRAS*, **445**, 3169
- Obergaulinger M., Just O., Janka H. T., Aloy M. A., Aloy C., 2014b, in Pogorelov N. V., Audit E., Zank G. P., eds, *Astronomical Society of the Pacific Conference Series Vol. 488, 8th International Conference of Numerical Modeling of Space Plasma Flows (ASTRONUM 2013)*. p. 255
- Obergaulinger M., Just O., Aloy M. A., 2018, *Journal of Physics G Nuclear Physics*, **45**, 084001
- Panagia N., 2003, *arXiv e-prints*, pp astro-ph/0309416
- Panov I. V., Kolbe E., Pfeiffer B., Rauscher T., Kratz K.-L., Thielemann F.-K., 2005, *Nuclear Physics A*, **747**, 633
- Panov I. V., Korneev I. Y., Rauscher T., Martínez-Pinedo G., Kelić-Heil A., Zinner N. T., Thielemann F.-K., 2010, *A&A*, **513**, A61
- Pian E., et al., 2017, *Nature*, **551**, 67
- Podsiadlowski P., 1992, *PASP*, **104**, 717
- Pruet J., Hoffman R. D., Woosley S. E., Janka H.-T., Buras R., 2006, *ApJ*, **644**, 1028
- Qian Y. Z., Wasserburg G. J., 2001, *ApJ*, **559**, 925
- Qian Y. Z., Wasserburg G. J., 2007, *Phys. Rep.*, **442**, 237
- Qian Y. Z., Wasserburg G. J., 2008, *ApJ*, **687**, 272
- Qian Y. Z., Woosley S. E., 1996, *ApJ*, **471**, 331
- Qian Y. Z., Vogel P., Wasserburg G. J., 1998, *ApJ*, **506**, 868
- Rampp M., Janka H.-T., 2002, *A&A*, **396**, 361
- Rando R., 2017, *Journal of Instrumentation*, **12**, C11024
- Rauscher T., Heger A., Hoffman R. D., Woosley S. E., 2002, *ApJ*, **576**, 323
- Rembiasz T., Obergaulinger M., Cerdá-Durán P., Müller E., Aloy M. A., 2016a, *MNRAS*, **456**, 3782
- Rembiasz T., Guilet J., Obergaulinger M., Cerdá-Durán P., Aloy M. A., Müller E., 2016b, *MNRAS*, **460**, 3316
- Ripley J. L., Metzger B. D., Arcones A., Martínez-Pinedo G., 2014, *MNRAS*, **438**, 3243
- Roederer I. U., Cowan J. J., Karakas A. I., Kratz K.-L., Lugaro M., Simmerer J., Farouqi K., Sneden C., 2010, *ApJ*, **724**, 975
- Roederer I. U., Preston G. W., Thompson I. B., Shectman S. A., Sneden C., Burley G. S., Kelson D. D., 2014, *AJ*, **147**, 136
- Saruwatari M., Hashimoto M.-a., Fukuda R., Fujimoto S.-i., 2013, *Journal of Astrophysics*, 2013, 1
- Seitenzahl I. R., Timmes F. X., Magkotsios G., 2014, *ApJ*, **792**, 10
- Siegel D. M., Barnes J., Metzger B. D., 2019, *Nature*, **569**, 241
- Smartt S. J., et al., 2017, *Nature*, **551**, 75
- Sneden C., McWilliam A., Preston G. W., Cowan J. J., Burris D. L., Armosky B. J., 1996, *ApJ*, **467**, 819
- Sneden C., Cowan J. J., Gallino R., 2008, *ARA&A*, **46**, 241
- Spruit H. C., 2002, *A&A*, **381**, 923
- Sukhbold T., Ertl T., Woosley S. E., Brown J. M., Janka H. T., 2016, *ApJ*, **821**, 38
- Surman R., McLaughlin G. C., 2004, *ApJ*, **603**, 611
- Surman R., McLaughlin G. C., Hix W. R., 2006, *ApJ*, **643**, 1057
- Suwa Y., Takiwaki T., Kotake K., Sato K., 2007, *PASJ*, **59**, 771
- Tanvir N. R., et al., 2017, *ApJ*, **848**, L27
- Thielemann F.-K., Nomoto K., Hashimoto M.-A., 1996, *ApJ*, **460**, 408
- Thompson T. A., Burrows A., Meyer B. S., 2001, *ApJ*, **562**, 887
- Tominaga N., 2009, *ApJ*, **690**, 526
- Tuli J., 2011, *Nuclear Wallet Cards*. 8th Edition, National Nuclear Data Center, Brookhaven National Laboratory, New York, <http://www.nndc.bnl.gov/wallet/wc8.html>
- Umeda H., Nomoto K., 2008, *ApJ*, **673**, 1014
- Wanajo S., 2006, *ApJ*, **647**, 1323
- Wanajo S., Janka H.-T., Müller B., 2011, *ApJ*, **726**, L15
- Wanajo S., Müller B., Janka H.-T., Heger A., 2018, *ApJ*, **852**, 40
- Wang W., Li Z., 2016, *ApJ*, **825**, 102
- Weinberger C., Diehl R., Pleintinger M. M. M., Siegt T., Greiner J., 2020, *A&A*, **638**, A83
- Wheeler J. C., Meier D. L., Wilson J. R., 2002, *ApJ*, **568**, 807
- Winteler C., 2012, dissertation, University of Basel

- Winteler C., Käppeli R., Perego A., Arcones A., Vasset N., Nishimura N.,
 Liebendörfer M., Thielemann F.-K., 2012, [ApJ](#), **750**, L22
- Woosley S. E., Bloom J. S., 2006, [ARA&A](#), **44**, 507
- Woosley S. E., Heger A., 2006, [ApJ](#), **637**, 914
- Woosley S. E., Heger A., 2007, [Phys. Rep.](#), **442**, 269
- Woosley S. E., Weaver T. A., 1995, [ApJS](#), **101**, 181
- Woosley S. E., Wilson J. R., Mathews G. J., Hoffman R. D., Meyer B. S.,
 1994, [ApJ](#), **433**, 229

APPENDIX A: DATA TABLES

The mass fractions after 1 Gyr can be found in Tables [A1](#), [A2](#), [A3](#), and [A4](#). We want to stress that, for the light elements, we provide only the contribution from the innermost part of the ejecta. The progenitor composition and late nucleosynthesis should be considered if supernova yields are needed for the lighter elements. All tables are also available online.

This paper has been typeset from a \LaTeX file prepared by the author.

Table A1. Mass fractions of individual isotopes for model 35OC-RO after 1 Gyr. The yields represent only the innermost part of the ejecta.

Isotope	X_i	Isotope	X_i	Isotope	X_i	Isotope	X_i	Isotope	X_i
¹ H	$2.74 \cdot 10^{-02}$	²⁸ Si	$3.88 \cdot 10^{-02}$	⁴⁸ Ti	$1.29 \cdot 10^{-03}$	⁶⁸ Zn	$2.48 \cdot 10^{-03}$	⁸⁵ Rb	$3.34 \cdot 10^{-05}$
² H	$6.95 \cdot 10^{-09}$	²⁹ Si	$5.63 \cdot 10^{-05}$	⁴⁹ Ti	$1.37 \cdot 10^{-04}$	⁷⁰ Zn	$5.44 \cdot 10^{-05}$	⁸⁷ Rb	$4.47 \cdot 10^{-05}$
³ He	$3.97 \cdot 10^{-08}$	³⁰ Si	$3.21 \cdot 10^{-04}$	⁵⁰ Ti	$3.01 \cdot 10^{-04}$	⁶⁹ Ga	$7.98 \cdot 10^{-05}$	⁸⁴ Sr	$2.05 \cdot 10^{-06}$
⁴ He	$1.46 \cdot 10^{-01}$	³¹ P	$1.07 \cdot 10^{-04}$	⁵¹ V	$1.17 \cdot 10^{-04}$	⁷¹ Ga	$1.77 \cdot 10^{-05}$	⁸⁶ Sr	$5.96 \cdot 10^{-06}$
⁷ Li	$2.60 \cdot 10^{-09}$	³² S	$1.93 \cdot 10^{-02}$	⁵⁰ Cr	$1.06 \cdot 10^{-04}$	⁷⁰ Ge	$1.01 \cdot 10^{-03}$	⁸⁷ Sr	$2.17 \cdot 10^{-06}$
⁷ Be	$4.97 \cdot 10^{-08}$	³³ S	$7.41 \cdot 10^{-05}$	⁵² Cr	$9.11 \cdot 10^{-04}$	⁷² Ge	$2.26 \cdot 10^{-04}$	⁸⁸ Sr	$6.74 \cdot 10^{-04}$
¹¹ B	$1.51 \cdot 10^{-09}$	³⁴ S	$3.90 \cdot 10^{-03}$	⁵³ Cr	$1.58 \cdot 10^{-04}$	⁷³ Ge	$1.04 \cdot 10^{-05}$	⁸⁹ Y	$6.93 \cdot 10^{-05}$
¹² C	$9.27 \cdot 10^{-03}$	³⁶ S	$3.31 \cdot 10^{-08}$	⁵⁴ Cr	$7.43 \cdot 10^{-04}$	⁷⁴ Ge	$1.01 \cdot 10^{-04}$	⁹⁰ Zr	$6.22 \cdot 10^{-04}$
¹³ C	$4.64 \cdot 10^{-08}$	³⁵ Cl	$1.12 \cdot 10^{-04}$	⁵⁵ Mn	$4.76 \cdot 10^{-04}$	⁷⁶ Ge	$4.32 \cdot 10^{-05}$	⁹¹ Zr	$4.77 \cdot 10^{-06}$
¹⁴ N	$7.43 \cdot 10^{-07}$	³⁷ Cl	$6.02 \cdot 10^{-05}$	⁵⁴ Fe	$2.36 \cdot 10^{-03}$	⁷⁵ As	$1.14 \cdot 10^{-05}$	⁹² Zr	$6.32 \cdot 10^{-08}$
¹⁵ N	$3.11 \cdot 10^{-06}$	³⁶ Ar	$3.64 \cdot 10^{-03}$	⁵⁶ Fe	$1.47 \cdot 10^{-01}$	⁷⁴ Se	$7.32 \cdot 10^{-05}$	⁹³ Nb	$1.09 \cdot 10^{-07}$
¹⁶ O	$3.40 \cdot 10^{-01}$	³⁸ Ar	$2.40 \cdot 10^{-03}$	⁵⁷ Fe	$4.18 \cdot 10^{-03}$	⁷⁶ Se	$1.09 \cdot 10^{-04}$	⁹² Mo	$7.16 \cdot 10^{-06}$
¹⁷ O	$1.34 \cdot 10^{-06}$	⁴⁰ Ar	$5.72 \cdot 10^{-09}$	⁵⁸ Fe	$2.78 \cdot 10^{-03}$	⁷⁷ Se	$1.19 \cdot 10^{-05}$	⁹⁴ Mo	$6.01 \cdot 10^{-08}$
¹⁸ O	$3.14 \cdot 10^{-08}$	³⁹ K	$1.83 \cdot 10^{-04}$	⁵⁹ Co	$1.97 \cdot 10^{-03}$	⁷⁸ Se	$1.23 \cdot 10^{-04}$	⁹⁵ Mo	$1.55 \cdot 10^{-09}$
¹⁹ F	$2.62 \cdot 10^{-09}$	⁴⁰ K	$1.49 \cdot 10^{-08}$	⁵⁸ Ni	$3.70 \cdot 10^{-02}$	⁸⁰ Se	$2.33 \cdot 10^{-04}$	⁹⁷ Mo	$1.26 \cdot 10^{-09}$
²⁰ Ne	$6.80 \cdot 10^{-02}$	⁴¹ K	$2.14 \cdot 10^{-05}$	⁶⁰ Ni	$4.90 \cdot 10^{-02}$	⁸² Se	$1.04 \cdot 10^{-04}$	⁹⁶ Ru	$9.43 \cdot 10^{-10}$
²¹ Ne	$1.17 \cdot 10^{-07}$	⁴⁰ Ca	$3.37 \cdot 10^{-03}$	⁶¹ Ni	$1.18 \cdot 10^{-03}$	⁷⁹ Br	$1.11 \cdot 10^{-05}$	⁹⁸ Ru	$3.26 \cdot 10^{-09}$
²² Ne	$2.14 \cdot 10^{-06}$	⁴² Ca	$2.53 \cdot 10^{-04}$	⁶² Ni	$2.96 \cdot 10^{-02}$	⁸¹ Br	$2.90 \cdot 10^{-05}$	⁹⁹ Ru	$4.84 \cdot 10^{-10}$
²³ Na	$8.86 \cdot 10^{-06}$	⁴³ Ca	$3.86 \cdot 10^{-05}$	⁶⁴ Ni	$9.14 \cdot 10^{-03}$	⁷⁸ Kr	$7.84 \cdot 10^{-06}$	¹⁰⁰ Ru	$3.94 \cdot 10^{-10}$
²⁴ Mg	$1.22 \cdot 10^{-02}$	⁴⁴ Ca	$2.07 \cdot 10^{-04}$	⁶³ Cu	$1.13 \cdot 10^{-03}$	⁸⁰ Kr	$2.57 \cdot 10^{-05}$	¹⁰¹ Ru	$3.89 \cdot 10^{-10}$
²⁵ Mg	$1.19 \cdot 10^{-06}$	⁴⁶ Ca	$1.48 \cdot 10^{-09}$	⁶⁵ Cu	$3.83 \cdot 10^{-04}$	⁸² Kr	$1.61 \cdot 10^{-05}$	¹⁰³ Rh	$1.92 \cdot 10^{-10}$
²⁶ Mg	$4.50 \cdot 10^{-08}$	⁴⁵ Sc	$4.70 \cdot 10^{-05}$	⁶⁴ Zn	$1.46 \cdot 10^{-02}$	⁸³ Kr	$5.04 \cdot 10^{-05}$	¹⁰² Pd	$5.34 \cdot 10^{-10}$
²⁶ Al	$7.07 \cdot 10^{-07}$	⁴⁶ Ti	$4.38 \cdot 10^{-05}$	⁶⁶ Zn	$1.32 \cdot 10^{-02}$	⁸⁴ Kr	$2.91 \cdot 10^{-04}$		
²⁷ Al	$1.56 \cdot 10^{-05}$	⁴⁷ Ti	$6.67 \cdot 10^{-05}$	⁶⁷ Zn	$1.45 \cdot 10^{-04}$	⁸⁶ Kr	$3.11 \cdot 10^{-04}$		

The table is also published in machine-readable format.

Table A2. Mass fractions of individual isotopes for model 35OC-Rw after 1 Gyr. The yields represent only the innermost part of the ejecta.

Isotope	X_i	Isotope	X_i	Isotope	X_i	Isotope	X_i	Isotope	X_i
¹ H	$1.19 \cdot 10^{-02}$	³⁷ Cl	$5.63 \cdot 10^{-05}$	⁶⁴ Ni	$1.96 \cdot 10^{-03}$	⁸⁶ Sr	$3.55 \cdot 10^{-06}$	¹¹² Cd	$1.11 \cdot 10^{-05}$
² H	$2.93 \cdot 10^{-07}$	³⁶ Ar	$4.00 \cdot 10^{-03}$	⁶³ Cu	$4.84 \cdot 10^{-04}$	⁸⁷ Sr	$2.14 \cdot 10^{-06}$	¹¹³ Cd	$2.11 \cdot 10^{-05}$
³ He	$6.29 \cdot 10^{-08}$	³⁸ Ar	$2.49 \cdot 10^{-03}$	⁶⁵ Cu	$1.50 \cdot 10^{-04}$	⁸⁸ Sr	$6.48 \cdot 10^{-04}$	¹¹⁴ Cd	$8.16 \cdot 10^{-06}$
⁴ He	$1.24 \cdot 10^{-01}$	⁴⁰ Ar	$2.38 \cdot 10^{-06}$	⁶⁴ Zn	$4.68 \cdot 10^{-03}$	⁸⁹ Y	$1.04 \cdot 10^{-04}$	¹¹⁶ Cd	$1.57 \cdot 10^{-05}$
⁷ Li	$4.21 \cdot 10^{-09}$	³⁹ K	$1.52 \cdot 10^{-04}$	⁶⁶ Zn	$4.41 \cdot 10^{-03}$	⁹⁰ Zr	$6.43 \cdot 10^{-04}$	¹¹⁵ In	$1.28 \cdot 10^{-06}$
⁷ Be	$2.34 \cdot 10^{-08}$	⁴⁰ K	$1.61 \cdot 10^{-05}$	⁶⁷ Zn	$9.22 \cdot 10^{-05}$	⁹¹ Zr	$5.59 \cdot 10^{-05}$	¹¹⁴ Sn	$9.85 \cdot 10^{-10}$
¹¹ B	$3.02 \cdot 10^{-06}$	⁴¹ K	$2.80 \cdot 10^{-05}$	⁶⁸ Zn	$1.42 \cdot 10^{-03}$	⁹² Zr	$8.49 \cdot 10^{-06}$	¹¹⁶ Sn	$1.44 \cdot 10^{-09}$
¹² C	$6.73 \cdot 10^{-03}$	⁴⁰ Ca	$4.08 \cdot 10^{-03}$	⁷⁰ Zn	$2.30 \cdot 10^{-04}$	⁹⁴ Zr	$2.00 \cdot 10^{-05}$	¹¹⁷ Sn	$2.48 \cdot 10^{-06}$
¹³ C	$4.92 \cdot 10^{-07}$	⁴² Ca	$2.52 \cdot 10^{-04}$	⁶⁹ Ga	$1.33 \cdot 10^{-04}$	⁹³ Nb	$6.78 \cdot 10^{-06}$	¹¹⁸ Sn	$4.11 \cdot 10^{-06}$
¹⁴ N	$4.04 \cdot 10^{-06}$	⁴³ Ca	$2.72 \cdot 10^{-05}$	⁷¹ Ga	$1.03 \cdot 10^{-04}$	⁹² Mo	$3.95 \cdot 10^{-05}$	¹¹⁹ Sn	$1.19 \cdot 10^{-06}$
¹⁵ N	$2.55 \cdot 10^{-05}$	⁴⁴ Ca	$2.61 \cdot 10^{-04}$	⁷⁰ Ge	$5.36 \cdot 10^{-04}$	⁹⁴ Mo	$1.76 \cdot 10^{-07}$	¹²⁰ Sn	$2.06 \cdot 10^{-06}$
¹⁶ O	$2.57 \cdot 10^{-01}$	⁴⁶ Ca	$3.85 \cdot 10^{-07}$	⁷² Ge	$2.26 \cdot 10^{-04}$	⁹⁵ Mo	$8.74 \cdot 10^{-06}$	¹²² Sn	$1.97 \cdot 10^{-06}$
¹⁷ O	$1.35 \cdot 10^{-05}$	⁴⁵ Sc	$2.33 \cdot 10^{-05}$	⁷³ Ge	$1.49 \cdot 10^{-04}$	⁹⁶ Mo	$9.07 \cdot 10^{-06}$	¹²⁴ Sn	$1.70 \cdot 10^{-06}$
¹⁸ O	$2.39 \cdot 10^{-08}$	⁴⁶ Ti	$2.63 \cdot 10^{-05}$	⁷⁴ Ge	$2.85 \cdot 10^{-04}$	⁹⁷ Mo	$1.25 \cdot 10^{-06}$	¹²¹ Sb	$7.15 \cdot 10^{-07}$
¹⁹ F	$1.13 \cdot 10^{-05}$	⁴⁷ Ti	$4.72 \cdot 10^{-05}$	⁷⁶ Ge	$5.96 \cdot 10^{-04}$	⁹⁸ Mo	$5.54 \cdot 10^{-06}$	¹²³ Sb	$1.38 \cdot 10^{-06}$
²⁰ Ne	$4.90 \cdot 10^{-02}$	⁴⁸ Ti	$4.10 \cdot 10^{-03}$	⁷⁵ As	$9.92 \cdot 10^{-05}$	¹⁰⁰ Mo	$1.44 \cdot 10^{-05}$	¹²² Te	$1.48 \cdot 10^{-09}$
²¹ Ne	$2.80 \cdot 10^{-05}$	⁴⁹ Ti	$1.39 \cdot 10^{-04}$	⁷⁴ Se	$4.87 \cdot 10^{-05}$	⁹⁶ Ru	$2.93 \cdot 10^{-09}$	¹²⁴ Te	$1.86 \cdot 10^{-09}$
²² Ne	$1.42 \cdot 10^{-06}$	⁵⁰ Ti	$1.24 \cdot 10^{-03}$	⁷⁶ Se	$5.98 \cdot 10^{-05}$	⁹⁸ Ru	$1.45 \cdot 10^{-09}$	¹²⁵ Te	$3.48 \cdot 10^{-06}$
²³ Na	$2.44 \cdot 10^{-05}$	⁵¹ V	$4.46 \cdot 10^{-04}$	⁷⁷ Se	$1.13 \cdot 10^{-04}$	⁹⁹ Ru	$1.20 \cdot 10^{-06}$	¹²⁶ Te	$1.43 \cdot 10^{-06}$
²⁴ Mg	$9.91 \cdot 10^{-03}$	⁵⁰ Cr	$5.65 \cdot 10^{-05}$	⁷⁸ Se	$3.04 \cdot 10^{-04}$	¹⁰⁰ Ru	$8.66 \cdot 10^{-09}$	¹²⁸ Te	$4.06 \cdot 10^{-06}$
²⁵ Mg	$4.93 \cdot 10^{-05}$	⁵² Cr	$1.71 \cdot 10^{-03}$	⁸⁰ Se	$1.81 \cdot 10^{-03}$	¹⁰¹ Ru	$1.76 \cdot 10^{-06}$	¹³⁰ Te	$2.02 \cdot 10^{-05}$
²⁶ Mg	$3.07 \cdot 10^{-06}$	⁵³ Cr	$8.76 \cdot 10^{-04}$	⁸² Se	$4.67 \cdot 10^{-03}$	¹⁰² Ru	$7.38 \cdot 10^{-06}$	¹²⁷ I	$2.35 \cdot 10^{-06}$
²⁶ Al	$5.16 \cdot 10^{-06}$	⁵⁴ Cr	$1.34 \cdot 10^{-03}$	⁷⁹ Br	$7.09 \cdot 10^{-04}$	¹⁰⁴ Ru	$1.85 \cdot 10^{-05}$	¹²⁹ Xe	$4.66 \cdot 10^{-06}$
²⁷ Al	$2.07 \cdot 10^{-04}$	⁵⁵ Mn	$1.59 \cdot 10^{-03}$	⁸¹ Br	$7.95 \cdot 10^{-04}$	¹⁰³ Rh	$8.95 \cdot 10^{-06}$	¹³⁰ Xe	$2.39 \cdot 10^{-10}$
²⁸ Si	$3.87 \cdot 10^{-02}$	⁵⁴ Fe	$2.94 \cdot 10^{-03}$	⁷⁸ Kr	$5.92 \cdot 10^{-06}$	¹⁰⁴ Pd	$3.53 \cdot 10^{-10}$	¹³¹ Xe	$4.96 \cdot 10^{-06}$
²⁹ Si	$1.30 \cdot 10^{-04}$	⁵⁶ Fe	$3.22 \cdot 10^{-01}$	⁸⁰ Kr	$1.37 \cdot 10^{-05}$	¹⁰⁵ Pd	$9.01 \cdot 10^{-06}$	¹³² Xe	$5.13 \cdot 10^{-04}$
³⁰ Si	$3.36 \cdot 10^{-04}$	⁵⁷ Fe	$1.53 \cdot 10^{-02}$	⁸² Kr	$1.08 \cdot 10^{-05}$	¹⁰⁶ Pd	$2.80 \cdot 10^{-05}$	¹³⁴ Xe	$4.20 \cdot 10^{-07}$
³¹ P	$1.97 \cdot 10^{-04}$	⁵⁸ Fe	$1.29 \cdot 10^{-03}$	⁸³ Kr	$4.90 \cdot 10^{-03}$	¹⁰⁸ Pd	$1.14 \cdot 10^{-06}$	¹³³ Cs	$3.37 \cdot 10^{-05}$
³² S	$2.03 \cdot 10^{-02}$	⁵⁹ Co	$1.80 \cdot 10^{-03}$	⁸⁴ Kr	$2.01 \cdot 10^{-03}$	¹¹⁰ Pd	$4.43 \cdot 10^{-06}$	¹³⁵ Ba	$7.26 \cdot 10^{-10}$
³³ S	$1.51 \cdot 10^{-04}$	⁵⁸ Ni	$4.14 \cdot 10^{-02}$	⁸⁶ Kr	$1.90 \cdot 10^{-04}$	¹⁰⁷ Ag	$6.46 \cdot 10^{-06}$		
³⁴ S	$4.10 \cdot 10^{-03}$	⁶⁰ Ni	$2.39 \cdot 10^{-02}$	⁸⁵ Rb	$1.99 \cdot 10^{-04}$	¹⁰⁹ Ag	$7.94 \cdot 10^{-07}$		
³⁶ S	$2.49 \cdot 10^{-06}$	⁶¹ Ni	$9.04 \cdot 10^{-04}$	⁸⁷ Rb	$6.57 \cdot 10^{-05}$	¹¹⁰ Cd	$2.44 \cdot 10^{-09}$		
³⁵ Cl	$1.48 \cdot 10^{-04}$	⁶² Ni	$1.12 \cdot 10^{-02}$	⁸⁴ Sr	$1.44 \cdot 10^{-06}$	¹¹¹ Cd	$1.78 \cdot 10^{-06}$		

The table is also published in machine-readable format.

Table A3. Mass fractions of individual isotopes for model 35OC-RRw after 1 Gyr. The yields represent only the innermost part of the ejecta.

Isotope	X_i	Isotope	X_i	Isotope	X_i	Isotope	X_i	Isotope	X_i
¹ H	$3.40 \cdot 10^{-02}$	²⁷ Al	$1.41 \cdot 10^{-03}$	⁴⁶ Ti	$1.24 \cdot 10^{-04}$	⁶⁴ Zn	$6.56 \cdot 10^{-03}$	⁸² Kr	$5.56 \cdot 10^{-06}$
² H	$7.76 \cdot 10^{-07}$	²⁸ Si	$1.51 \cdot 10^{-01}$	⁴⁷ Ti	$1.17 \cdot 10^{-04}$	⁶⁶ Zn	$1.68 \cdot 10^{-04}$	⁸³ Kr	$4.08 \cdot 10^{-06}$
³ He	$4.95 \cdot 10^{-07}$	²⁹ Si	$8.14 \cdot 10^{-04}$	⁴⁸ Ti	$3.28 \cdot 10^{-04}$	⁶⁷ Zn	$2.13 \cdot 10^{-04}$	⁸⁴ Kr	$1.72 \cdot 10^{-07}$
⁴ He	$2.11 \cdot 10^{-01}$	³⁰ Si	$2.57 \cdot 10^{-03}$	⁴⁹ Ti	$1.81 \cdot 10^{-04}$	⁶⁸ Zn	$1.21 \cdot 10^{-03}$	⁸⁶ Kr	$1.23 \cdot 10^{-08}$
⁷ Li	$3.52 \cdot 10^{-08}$	³¹ P	$1.78 \cdot 10^{-03}$	⁵⁰ Ti	$6.16 \cdot 10^{-06}$	⁷⁰ Zn	$6.44 \cdot 10^{-07}$	⁸⁵ Rb	$2.58 \cdot 10^{-06}$
⁷ Be	$1.24 \cdot 10^{-07}$	³² S	$5.96 \cdot 10^{-02}$	⁵¹ V	$2.14 \cdot 10^{-04}$	⁶⁹ Ga	$2.04 \cdot 10^{-04}$	⁸⁷ Rb	$1.61 \cdot 10^{-08}$
¹¹ B	$7.45 \cdot 10^{-07}$	³³ S	$1.01 \cdot 10^{-03}$	⁵⁰ Cr	$1.94 \cdot 10^{-04}$	⁷¹ Ga	$4.62 \cdot 10^{-05}$	⁸⁴ Sr	$2.62 \cdot 10^{-06}$
¹² C	$2.87 \cdot 10^{-04}$	³⁴ S	$3.79 \cdot 10^{-02}$	⁵² Cr	$1.61 \cdot 10^{-03}$	⁷⁰ Ge	$5.51 \cdot 10^{-05}$	⁸⁶ Sr	$1.10 \cdot 10^{-06}$
¹³ C	$4.97 \cdot 10^{-06}$	³⁶ S	$5.95 \cdot 10^{-05}$	⁵³ Cr	$3.91 \cdot 10^{-04}$	⁷² Ge	$2.14 \cdot 10^{-04}$	⁸⁷ Sr	$6.48 \cdot 10^{-07}$
¹⁴ N	$4.62 \cdot 10^{-06}$	³⁵ Cl	$2.53 \cdot 10^{-03}$	⁵⁴ Cr	$2.86 \cdot 10^{-04}$	⁷³ Ge	$5.72 \cdot 10^{-05}$	⁸⁸ Sr	$4.33 \cdot 10^{-07}$
¹⁵ N	$6.38 \cdot 10^{-05}$	³⁷ Cl	$2.84 \cdot 10^{-04}$	⁵⁵ Mn	$1.99 \cdot 10^{-03}$	⁷⁴ Ge	$3.16 \cdot 10^{-06}$	⁸⁹ Y	$2.44 \cdot 10^{-07}$
¹⁶ O	$1.62 \cdot 10^{-01}$	³⁶ Ar	$1.14 \cdot 10^{-02}$	⁵⁴ Fe	$3.04 \cdot 10^{-03}$	⁷⁶ Ge	$2.26 \cdot 10^{-07}$	⁹⁰ Zr	$3.99 \cdot 10^{-06}$
¹⁷ O	$1.80 \cdot 10^{-05}$	³⁸ Ar	$2.15 \cdot 10^{-02}$	⁵⁶ Fe	$2.13 \cdot 10^{-01}$	⁷⁵ As	$1.60 \cdot 10^{-05}$	⁹¹ Zr	$2.12 \cdot 10^{-06}$
¹⁸ O	$4.83 \cdot 10^{-08}$	⁴⁰ Ar	$5.76 \cdot 10^{-05}$	⁵⁷ Fe	$6.21 \cdot 10^{-03}$	⁷⁴ Se	$2.27 \cdot 10^{-05}$	⁹² Zr	$6.27 \cdot 10^{-08}$
¹⁹ F	$8.74 \cdot 10^{-06}$	³⁹ K	$1.72 \cdot 10^{-03}$	⁵⁸ Fe	$2.22 \cdot 10^{-04}$	⁷⁶ Se	$4.30 \cdot 10^{-05}$	⁹³ Nb	$2.85 \cdot 10^{-06}$
²⁰ Ne	$2.49 \cdot 10^{-03}$	⁴⁰ K	$2.81 \cdot 10^{-04}$	⁵⁹ Co	$1.71 \cdot 10^{-03}$	⁷⁷ Se	$2.33 \cdot 10^{-05}$	⁹² Mo	$1.21 \cdot 10^{-04}$
²¹ Ne	$4.28 \cdot 10^{-06}$	⁴¹ K	$1.26 \cdot 10^{-04}$	⁵⁸ Ni	$4.29 \cdot 10^{-03}$	⁷⁸ Se	$6.72 \cdot 10^{-06}$	⁹⁴ Mo	$4.93 \cdot 10^{-07}$
²² Ne	$2.23 \cdot 10^{-06}$	⁴⁰ Ca	$7.47 \cdot 10^{-03}$	⁶⁰ Ni	$2.83 \cdot 10^{-02}$	⁸⁰ Se	$2.63 \cdot 10^{-07}$	⁹⁵ Mo	$7.30 \cdot 10^{-08}$
²³ Na	$4.05 \cdot 10^{-05}$	⁴² Ca	$3.49 \cdot 10^{-03}$	⁶¹ Ni	$6.63 \cdot 10^{-04}$	⁸² Se	$1.39 \cdot 10^{-08}$	⁹⁶ Mo	$1.07 \cdot 10^{-09}$
²⁴ Mg	$1.01 \cdot 10^{-02}$	⁴³ Ca	$1.04 \cdot 10^{-04}$	⁶² Ni	$8.90 \cdot 10^{-04}$	⁷⁹ Br	$7.58 \cdot 10^{-06}$	⁹⁷ Mo	$1.62 \cdot 10^{-09}$
²⁵ Mg	$1.45 \cdot 10^{-04}$	⁴⁴ Ca	$3.59 \cdot 10^{-04}$	⁶⁴ Ni	$3.25 \cdot 10^{-05}$	⁸¹ Br	$9.38 \cdot 10^{-06}$	⁹⁶ Ru	$3.97 \cdot 10^{-08}$
²⁶ Mg	$1.05 \cdot 10^{-05}$	⁴⁶ Ca	$9.06 \cdot 10^{-08}$	⁶³ Cu	$1.02 \cdot 10^{-03}$	⁷⁸ Kr	$9.56 \cdot 10^{-06}$	⁹⁸ Ru	$2.44 \cdot 10^{-10}$
²⁶ Al	$1.23 \cdot 10^{-05}$	⁴⁵ Sc	$9.51 \cdot 10^{-05}$	⁶⁵ Cu	$4.26 \cdot 10^{-04}$	⁸⁰ Kr	$9.27 \cdot 10^{-06}$		

The table is also published in machine-readable format.

Table A4. Mass fractions of individual isotopes for model 35OC-Rs after 1 Gyr. The yields represent only the innermost part of the ejecta.

Isotope	X_i	Isotope	X_i	Isotope	X_i	Isotope	X_i	Isotope	X_i
¹ H	$9.57 \cdot 10^{-04}$	⁵⁰ Ti	$3.06 \cdot 10^{-02}$	⁸⁵ Rb	$1.15 \cdot 10^{-03}$	¹²⁶ Te	$3.39 \cdot 10^{-04}$	¹⁷² Yb	$1.75 \cdot 10^{-05}$
⁴ He	$2.64 \cdot 10^{-02}$	⁵¹ V	$4.17 \cdot 10^{-03}$	⁸⁷ Rb	$4.82 \cdot 10^{-04}$	¹²⁸ Te	$8.52 \cdot 10^{-04}$	¹⁷³ Yb	$2.43 \cdot 10^{-05}$
⁷ Be	$1.36 \cdot 10^{-10}$	⁵⁰ Cr	$5.60 \cdot 10^{-05}$	⁸⁴ Sr	$4.24 \cdot 10^{-07}$	¹³⁰ Te	$3.49 \cdot 10^{-03}$	¹⁷⁴ Yb	$2.88 \cdot 10^{-05}$
¹² C	$4.79 \cdot 10^{-03}$	⁵² Cr	$5.13 \cdot 10^{-03}$	⁸⁶ Sr	$2.42 \cdot 10^{-06}$	¹²⁷ I	$3.17 \cdot 10^{-04}$	¹⁷⁶ Yb	$1.04 \cdot 10^{-05}$
¹³ C	$5.94 \cdot 10^{-10}$	⁵³ Cr	$1.65 \cdot 10^{-02}$	⁸⁷ Sr	$8.25 \cdot 10^{-06}$	¹²⁹ Xe	$1.86 \cdot 10^{-03}$	¹⁷⁵ Lu	$9.23 \cdot 10^{-06}$
¹⁴ N	$2.03 \cdot 10^{-07}$	⁵⁴ Cr	$9.32 \cdot 10^{-03}$	⁸⁸ Sr	$2.65 \cdot 10^{-03}$	¹³¹ Xe	$3.29 \cdot 10^{-03}$	¹⁷⁷ Hf	$5.85 \cdot 10^{-06}$
¹⁵ N	$4.48 \cdot 10^{-07}$	⁵⁵ Mn	$7.04 \cdot 10^{-04}$	⁸⁹ Y	$5.74 \cdot 10^{-04}$	¹³² Xe	$5.02 \cdot 10^{-03}$	¹⁷⁸ Hf	$1.37 \cdot 10^{-05}$
¹⁶ O	$2.46 \cdot 10^{-01}$	⁵⁴ Fe	$3.92 \cdot 10^{-03}$	⁹⁰ Zr	$5.44 \cdot 10^{-04}$	¹³⁴ Xe	$2.58 \cdot 10^{-04}$	¹⁷⁹ Hf	$9.21 \cdot 10^{-06}$
¹⁷ O	$4.56 \cdot 10^{-08}$	⁵⁶ Fe	$7.01 \cdot 10^{-02}$	⁹¹ Zr	$1.17 \cdot 10^{-04}$	¹³⁶ Xe	$2.32 \cdot 10^{-05}$	¹⁸⁰ Hf	$1.19 \cdot 10^{-05}$
¹⁸ O	$3.25 \cdot 10^{-06}$	⁵⁷ Fe	$5.13 \cdot 10^{-03}$	⁹² Zr	$7.59 \cdot 10^{-05}$	¹³³ Cs	$8.67 \cdot 10^{-04}$	¹⁸¹ Ta	$5.21 \cdot 10^{-06}$
¹⁹ F	$3.07 \cdot 10^{-06}$	⁵⁸ Fe	$1.49 \cdot 10^{-02}$	⁹⁴ Zr	$1.49 \cdot 10^{-04}$	¹³⁵ Ba	$1.32 \cdot 10^{-05}$	¹⁸² W	$8.61 \cdot 10^{-06}$
²⁰ Ne	$3.48 \cdot 10^{-02}$	⁵⁹ Co	$1.35 \cdot 10^{-03}$	⁹³ Nb	$2.81 \cdot 10^{-04}$	¹³⁷ Ba	$8.25 \cdot 10^{-06}$	¹⁸³ W	$1.32 \cdot 10^{-06}$
²¹ Ne	$6.38 \cdot 10^{-07}$	⁵⁸ Ni	$4.87 \cdot 10^{-02}$	⁹² Mo	$1.86 \cdot 10^{-06}$	¹³⁸ Ba	$3.19 \cdot 10^{-05}$	¹⁸⁴ W	$3.75 \cdot 10^{-06}$
²² Ne	$3.49 \cdot 10^{-06}$	⁶⁰ Ni	$2.93 \cdot 10^{-02}$	⁹⁴ Mo	$2.15 \cdot 10^{-08}$	¹³⁹ La	$7.63 \cdot 10^{-06}$	¹⁸⁶ W	$1.23 \cdot 10^{-06}$
²³ Na	$9.55 \cdot 10^{-06}$	⁶¹ Ni	$1.18 \cdot 10^{-03}$	⁹⁵ Mo	$1.44 \cdot 10^{-04}$	¹⁴⁰ Ce	$2.16 \cdot 10^{-06}$	¹⁸⁵ Re	$8.96 \cdot 10^{-07}$
²⁴ Mg	$1.17 \cdot 10^{-02}$	⁶² Ni	$4.59 \cdot 10^{-02}$	⁹⁶ Mo	$5.93 \cdot 10^{-05}$	¹⁴² Ce	$3.09 \cdot 10^{-06}$	¹⁸⁷ Re	$3.90 \cdot 10^{-07}$
²⁵ Mg	$8.32 \cdot 10^{-07}$	⁶⁴ Ni	$3.23 \cdot 10^{-02}$	⁹⁷ Mo	$4.43 \cdot 10^{-05}$	¹⁴¹ Pr	$2.04 \cdot 10^{-06}$	¹⁸⁷ Os	$6.27 \cdot 10^{-09}$
²⁶ Mg	$6.10 \cdot 10^{-07}$	⁶³ Cu	$1.38 \cdot 10^{-03}$	⁹⁸ Mo	$4.70 \cdot 10^{-05}$	¹⁴³ Nd	$3.89 \cdot 10^{-06}$	¹⁸⁸ Os	$1.26 \cdot 10^{-06}$
²⁶ Al	$9.52 \cdot 10^{-07}$	⁶⁵ Cu	$6.82 \cdot 10^{-04}$	¹⁰⁰ Mo	$6.90 \cdot 10^{-05}$	¹⁴⁴ Nd	$2.80 \cdot 10^{-06}$	¹⁸⁹ Os	$9.44 \cdot 10^{-07}$
²⁷ Al	$2.99 \cdot 10^{-05}$	⁶⁴ Zn	$6.26 \cdot 10^{-03}$	⁹⁹ Ru	$1.43 \cdot 10^{-05}$	¹⁴⁵ Nd	$6.31 \cdot 10^{-06}$	¹⁹⁰ Os	$1.12 \cdot 10^{-06}$
²⁸ Si	$4.95 \cdot 10^{-02}$	⁶⁶ Zn	$3.98 \cdot 10^{-02}$	¹⁰¹ Ru	$4.42 \cdot 10^{-05}$	¹⁴⁶ Nd	$3.28 \cdot 10^{-06}$	¹⁹² Os	$1.45 \cdot 10^{-06}$
²⁹ Si	$6.58 \cdot 10^{-05}$	⁶⁷ Zn	$1.04 \cdot 10^{-03}$	¹⁰² Ru	$1.71 \cdot 10^{-04}$	¹⁴⁸ Nd	$5.77 \cdot 10^{-06}$	¹⁹¹ Ir	$5.36 \cdot 10^{-07}$
³⁰ Si	$4.11 \cdot 10^{-04}$	⁶⁸ Zn	$1.78 \cdot 10^{-02}$	¹⁰⁴ Ru	$3.59 \cdot 10^{-04}$	¹⁵⁰ Nd	$5.48 \cdot 10^{-06}$	¹⁹³ Ir	$1.81 \cdot 10^{-06}$
³¹ P	$1.34 \cdot 10^{-04}$	⁷⁰ Zn	$5.67 \cdot 10^{-03}$	¹⁰³ Rh	$4.19 \cdot 10^{-04}$	¹⁴⁷ Sm	$6.73 \cdot 10^{-06}$	¹⁹⁴ Pt	$7.86 \cdot 10^{-06}$
³² S	$2.21 \cdot 10^{-02}$	⁶⁹ Ga	$1.72 \cdot 10^{-03}$	¹⁰⁵ Pd	$3.50 \cdot 10^{-04}$	¹⁴⁹ Sm	$3.15 \cdot 10^{-06}$	¹⁹⁵ Pt	$1.56 \cdot 10^{-05}$
³³ S	$8.62 \cdot 10^{-05}$	⁷¹ Ga	$6.98 \cdot 10^{-04}$	¹⁰⁶ Pd	$1.77 \cdot 10^{-04}$	¹⁵² Sm	$7.49 \cdot 10^{-06}$	¹⁹⁶ Pt	$3.89 \cdot 10^{-05}$
³⁴ S	$7.66 \cdot 10^{-03}$	⁷⁰ Ge	$3.80 \cdot 10^{-04}$	¹⁰⁸ Pd	$1.83 \cdot 10^{-04}$	¹⁵⁴ Sm	$6.94 \cdot 10^{-06}$	¹⁹⁸ Pt	$1.02 \cdot 10^{-04}$
³⁶ S	$2.19 \cdot 10^{-07}$	⁷² Ge	$3.56 \cdot 10^{-03}$	¹¹⁰ Pd	$2.45 \cdot 10^{-04}$	¹⁵¹ Eu	$8.28 \cdot 10^{-06}$	¹⁹⁷ Au	$2.72 \cdot 10^{-05}$
³⁵ Cl	$1.37 \cdot 10^{-04}$	⁷³ Ge	$1.70 \cdot 10^{-03}$	¹⁰⁷ Ag	$2.49 \cdot 10^{-04}$	¹⁵³ Eu	$5.07 \cdot 10^{-06}$	¹⁹⁹ Hg	$3.54 \cdot 10^{-05}$
³⁷ Cl	$2.85 \cdot 10^{-05}$	⁷⁴ Ge	$2.99 \cdot 10^{-03}$	¹⁰⁹ Ag	$2.19 \cdot 10^{-04}$	¹⁵⁵ Gd	$5.34 \cdot 10^{-06}$	²⁰⁰ Hg	$7.01 \cdot 10^{-06}$
³⁶ Ar	$4.28 \cdot 10^{-03}$	⁷⁶ Ge	$6.00 \cdot 10^{-03}$	¹¹⁰ Cd	$1.03 \cdot 10^{-10}$	¹⁵⁶ Gd	$8.01 \cdot 10^{-06}$	²⁰¹ Hg	$2.52 \cdot 10^{-07}$
³⁸ Ar	$4.20 \cdot 10^{-03}$	⁷⁵ As	$2.60 \cdot 10^{-03}$	¹¹¹ Cd	$2.41 \cdot 10^{-04}$	¹⁵⁷ Gd	$7.71 \cdot 10^{-06}$	²⁰² Hg	$1.75 \cdot 10^{-08}$
⁴⁰ Ar	$1.13 \cdot 10^{-07}$	⁷⁴ Se	$1.97 \cdot 10^{-05}$	¹¹² Cd	$2.20 \cdot 10^{-04}$	¹⁵⁸ Gd	$1.23 \cdot 10^{-05}$	²⁰⁴ Hg	$2.31 \cdot 10^{-09}$
³⁹ K	$1.13 \cdot 10^{-04}$	⁷⁶ Se	$4.53 \cdot 10^{-05}$	¹¹³ Cd	$2.62 \cdot 10^{-04}$	¹⁶⁰ Gd	$1.40 \cdot 10^{-05}$	²⁰³ Tl	$3.23 \cdot 10^{-09}$
⁴⁰ K	$2.19 \cdot 10^{-08}$	⁷⁷ Se	$3.40 \cdot 10^{-03}$	¹¹⁴ Cd	$3.02 \cdot 10^{-04}$	¹⁵⁹ Tb	$8.26 \cdot 10^{-06}$	²⁰⁵ Tl	$1.72 \cdot 10^{-10}$
⁴¹ K	$5.64 \cdot 10^{-06}$	⁷⁸ Se	$5.27 \cdot 10^{-03}$	¹¹⁶ Cd	$8.83 \cdot 10^{-05}$	¹⁶¹ Dy	$1.29 \cdot 10^{-05}$	²⁰⁶ Pb	$1.32 \cdot 10^{-08}$
⁴⁰ Ca	$3.50 \cdot 10^{-03}$	⁸⁰ Se	$2.08 \cdot 10^{-02}$	¹¹⁵ In	$5.19 \cdot 10^{-05}$	¹⁶² Dy	$3.54 \cdot 10^{-05}$	²⁰⁷ Pb	$1.12 \cdot 10^{-08}$
⁴² Ca	$6.87 \cdot 10^{-04}$	⁸² Se	$3.05 \cdot 10^{-02}$	¹¹⁷ Sn	$1.21 \cdot 10^{-04}$	¹⁶³ Dy	$3.90 \cdot 10^{-05}$	²⁰⁸ Pb	$1.18 \cdot 10^{-08}$
⁴³ Ca	$9.00 \cdot 10^{-06}$	⁷⁹ Br	$7.80 \cdot 10^{-03}$	¹¹⁸ Sn	$7.49 \cdot 10^{-05}$	¹⁶⁴ Dy	$4.87 \cdot 10^{-05}$	²⁰⁹ Bi	$8.00 \cdot 10^{-09}$
⁴⁴ Ca	$5.73 \cdot 10^{-05}$	⁸¹ Br	$2.40 \cdot 10^{-02}$	¹¹⁹ Sn	$4.70 \cdot 10^{-05}$	¹⁶⁵ Ho	$2.08 \cdot 10^{-05}$	²³² Th	$3.57 \cdot 10^{-09}$
⁴⁶ Ca	$4.87 \cdot 10^{-05}$	⁷⁸ Kr	$1.91 \cdot 10^{-06}$	¹²⁰ Sn	$5.17 \cdot 10^{-05}$	¹⁶⁶ Er	$3.47 \cdot 10^{-05}$	²³⁵ U	$8.07 \cdot 10^{-10}$
⁴⁵ Sc	$6.78 \cdot 10^{-06}$	⁸⁰ Kr	$5.56 \cdot 10^{-06}$	¹²² Sn	$3.21 \cdot 10^{-05}$	¹⁶⁷ Er	$3.72 \cdot 10^{-05}$	²³⁸ U	$9.01 \cdot 10^{-10}$
⁴⁶ Ti	$2.44 \cdot 10^{-05}$	⁸² Kr	$7.64 \cdot 10^{-06}$	¹²⁴ Sn	$2.59 \cdot 10^{-05}$	¹⁶⁸ Er	$2.23 \cdot 10^{-05}$		
⁴⁷ Ti	$5.68 \cdot 10^{-05}$	⁸³ Kr	$1.19 \cdot 10^{-02}$	¹²¹ Sb	$4.93 \cdot 10^{-05}$	¹⁷⁰ Er	$1.27 \cdot 10^{-05}$		
⁴⁸ Ti	$2.71 \cdot 10^{-02}$	⁸⁴ Kr	$8.11 \cdot 10^{-03}$	¹²³ Sb	$3.23 \cdot 10^{-05}$	¹⁶⁹ Tm	$8.59 \cdot 10^{-06}$		
⁴⁹ Ti	$1.31 \cdot 10^{-03}$	⁸⁶ Kr	$2.40 \cdot 10^{-03}$	¹²⁵ Te	$8.69 \cdot 10^{-05}$	¹⁷¹ Yb	$9.76 \cdot 10^{-06}$		

The table is also published in machine-readable format.